An acidic microenvironment sets the humoral pattern recognition molecule PTX3 in a tissue repair mode

Andrea Doni,[1] Tiziana Musso,[2] Diego Morone,[1] Antonio Bastone,[3] Vanessa Zambelli,[4] Marina Sironi,[1] Carlotta Castagnoli,[5] Irene Cambieri,[5] Matteo Stravalaci,[3] Fabio Pasqualini,[1] Ilaria Laface,[1] Sonia Valentino,[1] Silvia Tartari,[1] Andrea Ponzetta,[1] Virginia Maina,[1] Silvia S. Barbieri,[6] Elena Tremoli,[6,7] Alberico L. Catapano,[7,8] Giuseppe D. Norata,[7,9] Barbara Bottazzi,[1] Cecilia Garlanda,[1] and Alberto Mantovani[1,10]

[1]Istituto di Ricovero e Cura a Carattere Scientifico (IRCCS) - Humanitas Clinical and Research Center, 20089 Milan, Italy
[2]Department of Public Health and Microbiology, University of Turin, 10124 Turin, Italy
[3]Department of Molecular Biochemistry and Pharmachology, IRCCS - Istituto di Ricerche Farmacologiche Mario Negri, 20156 Milan, Italy
[4]Department of Health Science, University of Milano-Bicocca, 20126 Monza, Italy
[5]Department of Plastic Surgery, Burn Unit and Skin Bank, Centro Traumatologico Ortopedico (CTO) Hospital, 10126 Turin, Italy
[6]IRCCS - Centro Cardiologico Monzino, 20138 Milan, Italy
[7]Department of Pharmacological and Biomolecular Sciences, University of Milan, 20122 Milan, Italy
[8]IRCCS - Multimedica, 20099 Milan, Italy
[9]Società Italiana per lo Studio della Arteriosclerosi (SISA) Center for the Study of Atherosclerosis, Bassini Hospital, 20154 Milan, Italy
[10]Humanitas University, 20089 Milan, Italy

Pentraxin 3 (PTX3) is a fluid-phase pattern recognition molecule and a key component of the humoral arm of innate immunity. In four different models of tissue damage in mice, PTX3 deficiency was associated with increased fibrin deposition and persistence, and thicker clots, followed by increased collagen deposition, when compared with controls. *Ptx3*-deficient macrophages showed defective pericellular fibrinolysis in vitro. PTX3-bound fibrinogen/fibrin and plasminogen at acidic pH and increased plasmin-mediated fibrinolysis. The second exon-encoded N-terminal domain of PTX3 recapitulated the activity of the intact molecule. Thus, a prototypic component of humoral innate immunity, PTX3, plays a nonredundant role in the orchestration of tissue repair and remodeling. Tissue acidification resulting from metabolic adaptation during tissue repair sets PTX3 in a tissue remodeling and repair mode, suggesting that matrix and microbial recognition are common, ancestral features of the humoral arm of innate immunity.

CORRESPONDENCE
Alberto Mantovani:
alberto.mantovani@humanitasresearch.it

Abbreviations used: α-SMA, α-smooth muscle actin; BCECF, 2′,7′-Bis-(2-Carboxyethyl)-5-(and-6)-Carboxyfluorescein; CRP, C reactive protein; DCA, dichloroacetate; ECM, extracellular matrix; FAP, fibroblast activation protein; FG, fibrinogen; MPO, myeloperoxidase; PDGFR, platelet-derived growth factor receptor; Plg, plasminogen; PRM, pattern recognition molecule; PTX3, Pentraxin 3; SPR, surface plasmon resonance; tPA, tissue plasminogen activator; TRAP, thrombin receptor agonist peptide-6; uPA, urokinase plasminogen activator; uPAR, uPA receptor.

Innate immunity represents a first line of resistance against pathogens and is a key determinant of the activation and orientation of adaptive immunity. Innate immunity is also responsible for the activation of the inflammatory and reparative responses in sterile tissue injury (Medzhitov, 2008). The innate immune system includes a cellular and a humoral arm (Medzhitov, 2008; Bottazzi et al., 2010). Humoral fluid phase pattern recognition molecules (PRMs) are diverse and include components of the complement cascade, ficolins, collectins, and pentraxins (Holmskov et al., 2003; Pepys and Hirschfield, 2003; Bottazzi et al., 2010).

The long pentraxin 3 (PTX3) is a prototypic fluid-phase humoral PRM that acts as an essential component of the humoral arm of innate immunity (Garlanda et al., 2002; Bottazzi et al., 2010; Cunha et al., 2014). PTX3 is an octameric glycoprotein made of a C-terminal pentraxin-like domain and of an unrelated N-terminal domain, rapidly produced by myelomonocytic and stromal cells, including endothelial cells, fibroblasts, and smooth muscle cells, in response to primary proinflammatory cytokines, in particular IL-1, or TLRs, or rapidly released by neutrophils (Jaillon et al., 2007; Bottazzi et al., 2010).

The Rockefeller University Press $30.00
J. Exp. Med. 2015 Vol. 212 No. 6 905–925
www.jem.org/cgi/doi/10.1084/jem.20141268

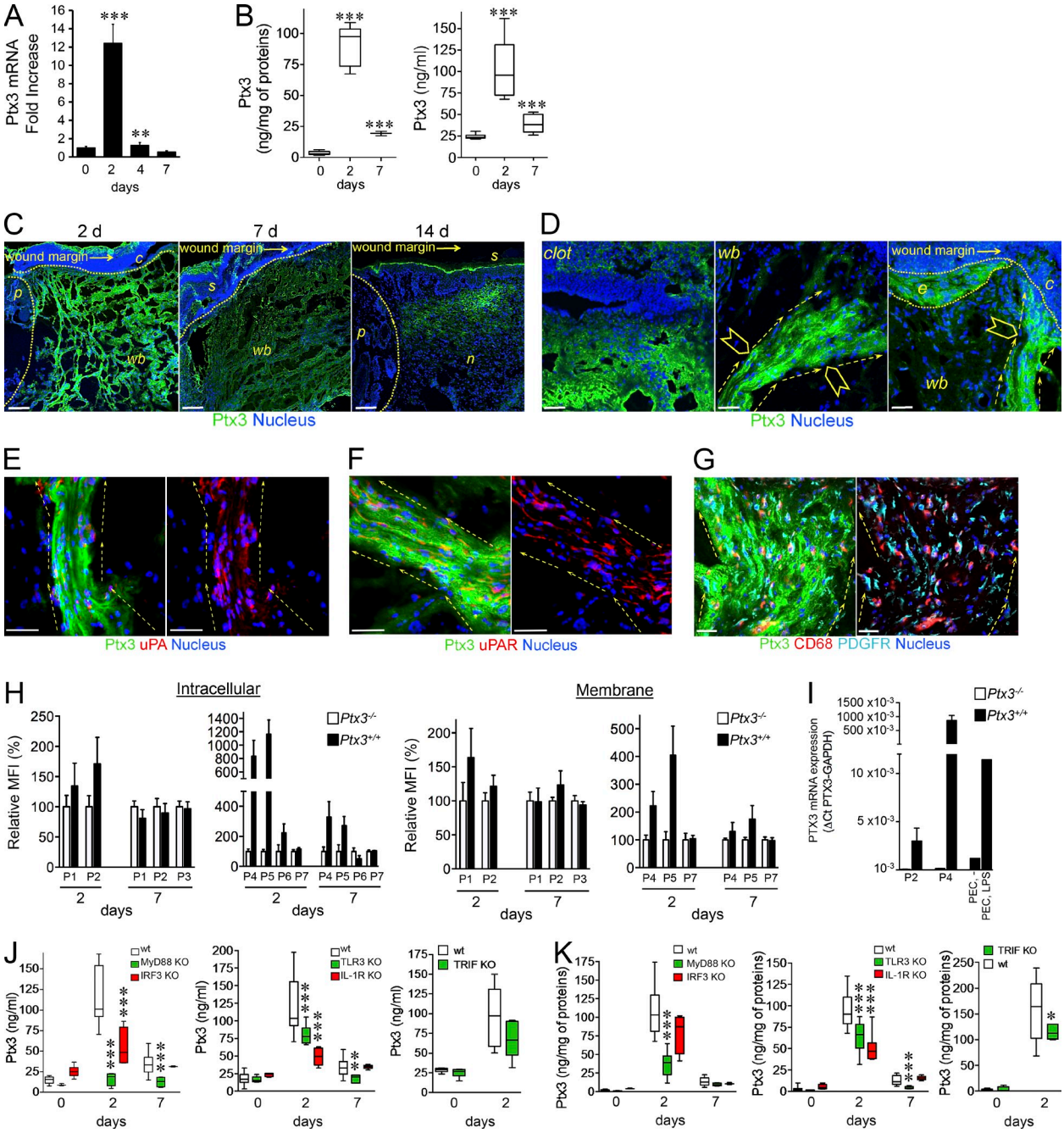

Figure 1. PTX3 is induced after skin wounding. A skin punch wound was generated on the back of mice. PTX3 mRNA expression was assessed by RT-PCR (A) and PTX3 local content and plasma levels (B) were measured after wounding in mice. (A) One representative experiment in triplicate ($n = 3$ independent mice/group) out of 2 is shown. (B) $n = 9$–11 independent mice. (C) Localization of PTX3 after skin wounding was assessed by confocal microscopy. Representative images are shown ($n = 39$ mice). C, clot; p, perilesion area; wb, wound bed; s, scab; n, neo-formed tissue. The analysis was performed at day 2, 7, and 14 after wounding. Bars, 100 µm. (D) Magnification images (40×) of PTX3 localization shown in C (10×) for clot (left) and damaged dermis (middle and right) 2 d after wounding. C, clot; wb, wound bed; e, epithelial outgrowth. Arrowheads denote cells invading the damaged dermis (middle) and the clot (right); dashed arrows show directionality of invading cells. Bar, 10 µm. (E–G) Cell populations (UPA$^+$ [E], UPAR$^+$ [F], PDGFR$^+$, and CD68$^+$ [G] cells) associated with PTX3 staining (green) were assessed by confocal microscopy (day 2 after wounding). Representative merged images (left) and indicated cell markers (red or cyan for PDGFR) with nucleus (blue; right) are shown. Dashed arrows show directionality of invading cells directed toward the wound bed. Bars, 10 µm. (E and F) $n = 6$ mice; (G) $n = 11$ mice. (H) Flow cytometry analysis of intracellular and membrane staining of PTX3 in leukocyte and stromal cell populations at 2 and 7 d after wounding of Ptx3$^{+/+}$ and Ptx3$^{-/-}$ mice. P1, CD45$^+$CD11b$^+$Ly6G$^+$; P2, CD45$^+$CD11b$^+$ Ly6C$^+$ F4/80; P3, CD45$^+$CD11b$^-$CD3$^+$; P4, CD45$^-$PDGFR$^+$; P5, CD45$^-$PDGFR$^+$FAP$^+$; P6, CD45$^-$α-SMA$^+$; P7, CD45$^-$C31$^+$. Values are expressed as relative percentage of MFI ± SD of Ptx3$^{+/+}$ cells (filled bars) compared with Ptx3$^{-/-}$ cells (open bars) used as a negative control. Data referring to P3 on day 2 after injury are not

PTX3 binds selected conserved microbial molecules and has antibody-like functions: it has opsonic activity via Fcγ receptors (Lu et al., 2008; Bottazzi et al., 2010), activates and regulates the complement cascade (Bottazzi et al., 2010; Ricklin and Lambris, 2013), and regulates inflammation (Bottazzi et al., 2010; Deban et al., 2010). Genetic evidence in mouse and man indicates that PTX3 is essential for resistance against selected pathogens, such as *Aspergillus fumigatus*, *Pseudomonas aeruginosa*, and *Klebsiella pneumoniae* (Garlanda et al., 2002; Bottazzi et al., 2010; Cunha et al., 2014; Jaillon et al., 2014), and plays a protective role in different conditions associated with tissue injury (Salio et al., 2008; Norata et al., 2009; Bottazzi et al., 2010; Deban et al., 2010).

Cellular sensors of tissue damage include TLRs and NOD-like receptors, which sense endogenous products of damaged cells and tissues, including extracellular matrix components and nucleic acids, and activate the production of inflammatory mediators and the recruitment of innate immune cells, such as macrophages and neutrophils, initiating tissue repair processes (Medzhitov, 2008). Components of the humoral arm of innate immunity involved in tissue damage, for instance in ischemia/reperfusion injury, include mannose-binding lectin and lectins, which upon binding altered host cells, promote activation of the lectin complement pathway contributing to tissue damage (Genster et al., 2014).

In the context of an effort aimed at dissecting the effector and regulatory function of PTX3 as a prototypic component of humoral innate immunity in tissue damage, we investigated its role in different tissue repair models. Here, we show that by interacting with the provisional matrix protein fibrin and with plasminogen, PTX3 plays a nonredundant protective role in the orchestration of tissue repair and remodeling.

RESULTS

Role of PTX3 in tissue repair

We investigated the role of PTX3 in models of tissue damage, including skin wounding, liver, and lung sterile tissue injury. A model of full-thickness excision dorsal skin wounding was first used. Wounding was associated with induction of increased levels of PTX3 mRNA and protein in the skin and blood (Fig. 1, A and B). By confocal microscopy analysis, on day 2 PTX3 was found in the clot and mostly associated with aligned bundles of cells migrating toward the wound site, and epithelial outgrowth (Fig. 1, C and D). On day 7, PTX3 was scattered in the scab and damaged dermis (Fig. 1 C). At healing (day 14), PTX3 expression was confined to neo-formed tissue and residual scab (Fig. 1 C). In particular, on day 2 PTX3 expression was associated with bundles of remodeling cells that collectively invaded the wound site, including urokinase plasminogen activator (uPA) positive (Fig. 1 E) and uPA receptor (uPAR) positive (Fig. 1 F) cells, $CD68^+$ macrophage-like cells and platelet-derived growth factor receptor $(PDGFR)^+$ fibroblasts and/or mesenchymal cells (Fig. 1 G). On day 2, PTX3 was detected by flow cytometry in neutrophils ($CD11b^+$ $Ly6G^+$), macrophages ($CD11b^+Ly6C^+F4/80^+$), and stromal cells, in particular $PDGFR\alpha^+$ mesenchymal cells, $PDGFR\alpha^+$/fibroblast activation $protein^+$ (FAP^+) reactive fibroblasts, and α-smooth muscle $actin^+$ (SMA^+) smooth muscle cells or myofibroblasts, and at low level in vascular endothelium ($CD31^+$; Fig. 1 H and Fig. S1). Expression of PTX3 was confirmed at the level of mRNA transcripts in sorted macrophages and mesenchymal cells (Fig. 1 I), but not in neutrophils that store preformed PTX3 in granules (Jaillon et al., 2007). On day 7, PTX3 was detected in $PDGFR\alpha^+$ and $PDGFR\alpha^+FAP^+$ mesenchymal stromal cells but not in leukocytes (Fig. 1 H). Neutrophils, macrophages, and $PDGFR\alpha^+$ mesenchymal cells also had PTX3 associated on the cell membrane in the course of the skin repair (Fig. 1 H), although, as shown by confocal images (Fig. 1, D–G), PTX3 was mainly associated with the pericellular matrix. Indeed, PTX3 is generally rapidly released from the cells, in particular by neutrophils (Jaillon et al., 2007).

TLRs and IL-1 are potent inducers of PTX3 and are involved in the orchestration of tissue repair (Medzhitov, 2008; Dinarello, 2009). It was therefore important to assess the pathways upstream of PTX3 in skin wound healing. Induction of PTX3 was almost completely abolished in blood and at the wound site in MyD88-deficient mice, whereas a partial reduction was observed in $Il1r^{-/-}$, $Tlr3^{-/-}$, $Irf3^{-/-}$, and $Ticam1^{-/-}$ mice (Fig. 1, J and K). These results suggest that induction of PTX3 is downstream of TLR sensing and IL-1 amplification, with the contribution of both MyD88- and TRIF-dependent pathways.

Early grossly evident acceleration of reduction of wound area was observed in $Ptx3^{-/-}$ mice (Fig. 2, A and B). Histological analysis revealed that $Ptx3^{-/-}$ mice had significantly thicker clots compared with controls (138.58 ± 25.8 μm and 78.59 ± 28.25 μm, in $Ptx3^{-/-}$ and WT mice, respectively; $P = 0.0001$; $n = 8$) on day 2, and thicker scabs (1,112.08 ± 189.13 μm compared with 645.09 ± 87.16 μm in WT mice; $P = 0.044$; $n = 8$) on day 7, characterized by excessive accumulation of eosinophilic material (Fig. 2 C) and fibrin (Fig. 2, D and E) throughout the observation time. In addition, an augmented content of factors (CD62P, TGFβ, PDGF, serotonin, CXCL1, and CXCL2) possibly derived from platelets

reported because of the low number of events acquired. $Ptx3^{+/+}$ (n = 7 independent mice), $Ptx3^{-/-}$ ($n = 6$ independent mice). (I) PTX3 mRNA expression was assessed in sorted macrophages (P2, $CD45^+$ $CD11b^+$ $Ly6C^+$ F4/80) and mesenchymal cells (P4, $CD45^-$ $PDGFR^+$) 2 d after wounding by quantitative RT-PCR. Results are presented as absolute values. Analysis of five $Ptx3^{+/+}$ and four $Ptx3^{-/-}$ independent mice was performed in triplicate. Peritoneal elicited cells (PEC), untreated or treated with LPS (10 ng/ml; 4 h), were used as control. (J and K) PTX3 plasma levels (J) and wound content (K) were measured in WT ($n = 11–14$) and MyD88- ($n = 6$), IRF3- ($n = 6$), TLR3- ($n = 8$), IL-1R1- ($n = 6$) and TRIF-deficient ($n = 6–7$) independent mice. Graphs show the mean ± SD (A, H, and I) or box plots (B, J, and K). *, $P < 0.05$; **, $P < 0.01$; and ***, $P < 0.005$ versus day 0 (A and B), or WT at the same time point (J and K; Mann-Whitney test).

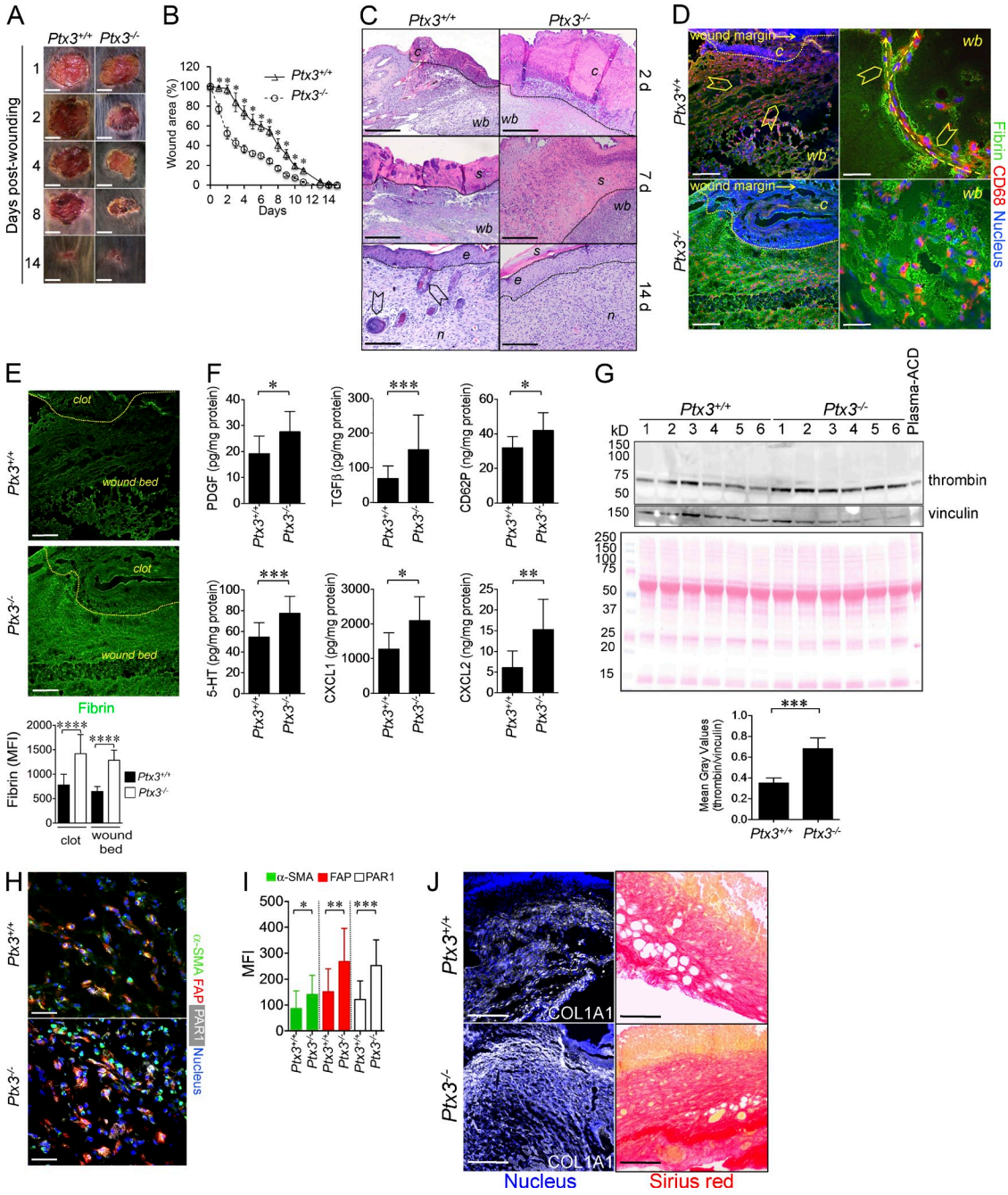

Figure 2. Skin repair is altered in PTX3-deficient mice. The skin wound healing model was used. (A) Representative macroscopic images of WT and *Ptx3*$^{-/-}$ skin wounds are shown at the indicated days after wounding. Bars, 5 mm. (B) Kinetic analysis of skin excisional wound areas was performed. Values represent mean ± SEM. *, P < 0.01 (Student's *t* test). One representative experiment (*n* = 10 mice/group) out of 15 is shown. (C) Representative histological images (H&E) of wound healing are shown for *Ptx3*$^{+/+}$ and *Ptx3*$^{-/-}$ mice at the indicated days after wounding. C, clot; wb, wound bed; s, scab; e, epithelialization; n, neo-formed tissue; arrowheads, hair follicles. Bars, 200 µm (2d, 7d) and 50 µm (14d). *n* = 8 mice. (D) Fibrin deposition and CD68^{+} invading cells in WT and *Ptx3*$^{-/-}$ wounds on day 2 were assessed by immunofluorescence confocal microscopy. Arrowheads: aligned CD68^{+} cells migrating toward the wound bed; right, dashed arrows: passages formed within the fibrin-rich wound site and directionality of invading CD68^{+} cells. C, clot; wb, wound bed. Representative images (*n* = 11 WT; *n* = 14 *Ptx3*$^{-/-}$ mice) are shown. Bars, 100 µm (left) and 10 µm (right). (E, left) Single fluorescence confocal microscopy images of fibrin (shown in D) are presented for *Ptx3*$^{+/+}$ and *Ptx3*$^{-/-}$ wounds on day 2. Bars, 100 µm. (right) fibrin staining quantification in the clot or in the wound bed is shown. Data are presented as mean ± SD; *n* = 2–3 10X images/mouse, 5 mice/group. ****, P < 0.0001, (Mann-Whitney test). (F) PDGF, TGFβ, CD62P, serotonin (5HT), CXCL1, and CXCL2 protein levels from WT and PTX3-deficient wound lysates after skin injury (day 1) were assessed by ELISA. Graphs show the mean ± SD. *, P < 0.05, **, P < 0.01 and ***, P < 0.005 versus WT (Mann-Whitney test); *n* = 8–10 independent mice/group. (G, top) Western blot analysis of thrombin in WT and PTX3-deficient wound lysates (day 1) was performed. Proteins, 20 µg/lane; mouse plasma-ACD, 1 µl/lane. Vinculin (middle) used as loading control and Ponceau red (bottom) staining are also shown. (bottom) Results are expressed as mean ± SD gray values of

(Nurden, 2011; Semple et al., 2011; Fig. 2 F), and thrombin (Fig. 2 G) were measured in PTX3-deficient wounds on day 1. Higher expression of markers of differentiated and activated fibroblasts was observed at day 2 (Fig. 2, H and I). Some of these factors (e.g., PDGF, TGFβ, serotonin, and thrombin) acting on stromal cells may well be responsible for increased early wound contraction and reduction of wound area observed in *Ptx3*$^{-/-}$ mice (Singer and Clark, 1999; Schäfer and Werner, 2008). Despite the accelerated reduction of wound area, PTX3 deficiency was associated with a defective reepithelialization at day 7 (the epithelial gap was 3,002 ± 432 µm and 1,306 ± 503 µm in *Ptx3*$^{-/-}$ and WT mice, respectively; P = 0.026; *n* = 7) and epithelial hyperplasia (10.8 ± 0.8 epithelial layers in *Ptx3*$^{-/-}$ vs. 6.0 ± 1.4 in WT mice; P = 0.0001; *n* = 8) and defective development of skin appendages at day 14, suggesting a defective mature tissue formation (Fig. 2 C). At later time points (25 d after wounding), the epithelial layers did not differ in the two groups (3.2 ± 1.1 epithelial layers in *Ptx3*$^{-/-}$ skins compared with 3.4 ± 1.3 in *Ptx3*$^{+/+}$ skins; *n* = 5), or in unwounded skins (unpublished data), indicating that epithelial hyperplasia associated with altered skin wound healing in PTX3-deficient mice was a transient event. Vascular density was not affected by PTX3 deficiency (day 2, 11 ± 7 vs. 17 ± 11; day 7, 42 ± 16 vs. 47 ± 16; day 14, 49 ± 17 vs. 43 ± 16 CD31$^+$ vessels/mm^2 in *Ptx3*$^{+/+}$ vs. *Ptx3*$^{-/-}$; *n* = 4–6; P = ns).

At the beginning of new tissue formation, remodeling cells enter the wound, allowing the replacement of the fibrin matrix by mature granulation tissue rich in type I collagen, as well as other extracellular matrix (ECM) proteins (Romer et al., 1996; de Giorgio-Miller et al., 2005). PTX3 deficiency was associated with alterations in the organization of remodeling cells invading the injured area. As previously shown (Singer and Clark, 1999), in WT mice, CD68$^+$ macrophages (Fig. 2 D) and PDGFRα$^+$ mesenchymal cells (not depicted) collectively migrated toward the wound bed and the clot, creating patent passages within fibrin matrix (Fig. 2 D). In *Ptx3*$^{-/-}$ mice, CD68$^+$ macrophages and PDGFRα$^+$ cells were scattered in the abundant fibrin-rich matrix and failed to create patent passages, suggesting defective directional migration and invasive phenotype (Fig. 2 D). Wound collagen was evaluated by collagen I and Sirius red staining. On day 7, collagen content was higher in *Ptx3*$^{-/-}$ tissues after wounding compared with WT (Fig. 2 J). Treatment with recombinant PTX3 reversed the phenotype of *Ptx3*$^{-/-}$ mice (Fig. 3, A–G) and had a significant effect on collagen deposition at one time point (day 7) in WT mice, suggesting that endogenous PTX3 is sufficient for gross biological function. The N-terminal domain, but not the C-terminal one, was necessary and sufficient to revert the phenotype (Fig. 3, A–G). Thus, after skin wounding, PTX3 deficiency was associated with increased clotting and excessive fibrin accumulation on day 2, followed by thicker scabs, augmented collagen deposition, and delayed reepithelialization on day 7, and epithelial hyperplasia and defective mature tissue formation on day 14, which are all signs of defective repair (Romer et al., 1996).

In an effort to extend these observations to models of sterile injury, we studied CCl_4-induced liver injury and acid-induced lung damage, in which genetic deficiencies causing prothrombotic responses are associated with impaired tissue remodeling and fibrosis (Pohl et al., 2001; Idell, 2003; Calvaruso et al., 2008). PTX3 plasma levels increased in the blood after acute liver injury (8–48 h), as well as chronic injury (6 wk), and returned toward basal levels at resolution of fibrosis (Fig. 4 A). PTX3 localized in necroinflammatory areas associated with GR1$^+$ cells (8–48 h), and in the portal tracts associated with uPA$^+$, PDGFR$^+$, and CD68$^+$ cells (6 wk; unpublished data). PTX3 deficiency did not affect necrosis (8–48 h; unpublished data); however, it was associated with an increased number of thrombosed centrolobular veins 8 h after CCl_4 injection (69.61 ± 17.16% in *Ptx3*$^{-/-}$ mice compared with 20.80 ± 8.46% in WT mice; *n* = 4; P = 0.011; Fig. 4 B); augmented deposits of eosinophilic material rich in fibrin in necroinflammatory areas of lobular spaces close to the centrolobular vein at 24 and 48 h, and in the portal tracts after chronic injury (6 wk; Fig. 4, B and C); augmented fibrosis assessed by measurement of liver α-SMA$^+$ immunoreactive area (Fig. 4 D); and OH-proline content (Fig. 4 E), Sirius red, and collagen I staining at portal septa (Fig. 4, F and G; 6 wk). Similarly, in the acid-induced lung injury model, we observed increased fibrin deposition at day 7 (Fig. 4 H) and increased collagen content at day 30 in *Ptx3*$^{-/-}$ mice (Fig. 4 I). Finally, PTX3-deficient mice were more susceptible to arterial thrombosis in a model of $FeCl_3$-induced vascular injury (Koschnick et al., 2005; Fig. 5 A), and exogenous PTX3 reversed the phenotype in *Ptx3*$^{-/-}$ mice and reduced the severity in *Ptx3*$^{+/+}$ mice (Fig. 5, B and C). These results suggest that in different models of tissue injury, PTX3 deficiency is associated with increased clotting and fibrin deposition and alteration of tissue repair, thus indicating that PTX3 has a protective role in tissue damage.

PTX3 binds P-selectin and has a negative regulatory function in selected models of inflammation (Bottazzi et al., 2010; Deban et al., 2010). Given the role of leukocytes in the orchestration of tissue repair, it was important to ascertain whether the altered wound healing observed in *Ptx3*$^{-/-}$ mice was in fact the expression of deregulated leukocyte recruitment. The analysis of leukocyte recruitment by immunohistochemistry, flow cytometry and confocal microscopy in skin and liver, and myeloperoxidase (MPO) content in skin wound lysates showed no difference in the total number of recruited cell populations (polymorphonuclear cells and macrophages) in the two groups

thrombin/vinculin. (*n* = 6 mice/group). ***, P < 0.005 (Mann-Whitney test). (H and I) Representative confocal microscopy immunofluorescence staining images (*left*) and quantification (*right*) of α-SMA (green), FAP (red) and PAR1 (white) in WT and PTX3-deficient wounds are shown. *, P < 0.05, **, P < 0.01 and ***, P < 0.005 versus WT (Student's *t* test); *n* = 3–4 20X images/mouse, (*n* = 4–7 mice/group). (J) Collagen I (COL1A1) and Sirius red staining in the wounds at day 7. Representative images are shown (*n* = 5 mice). Bars, 100 µm.

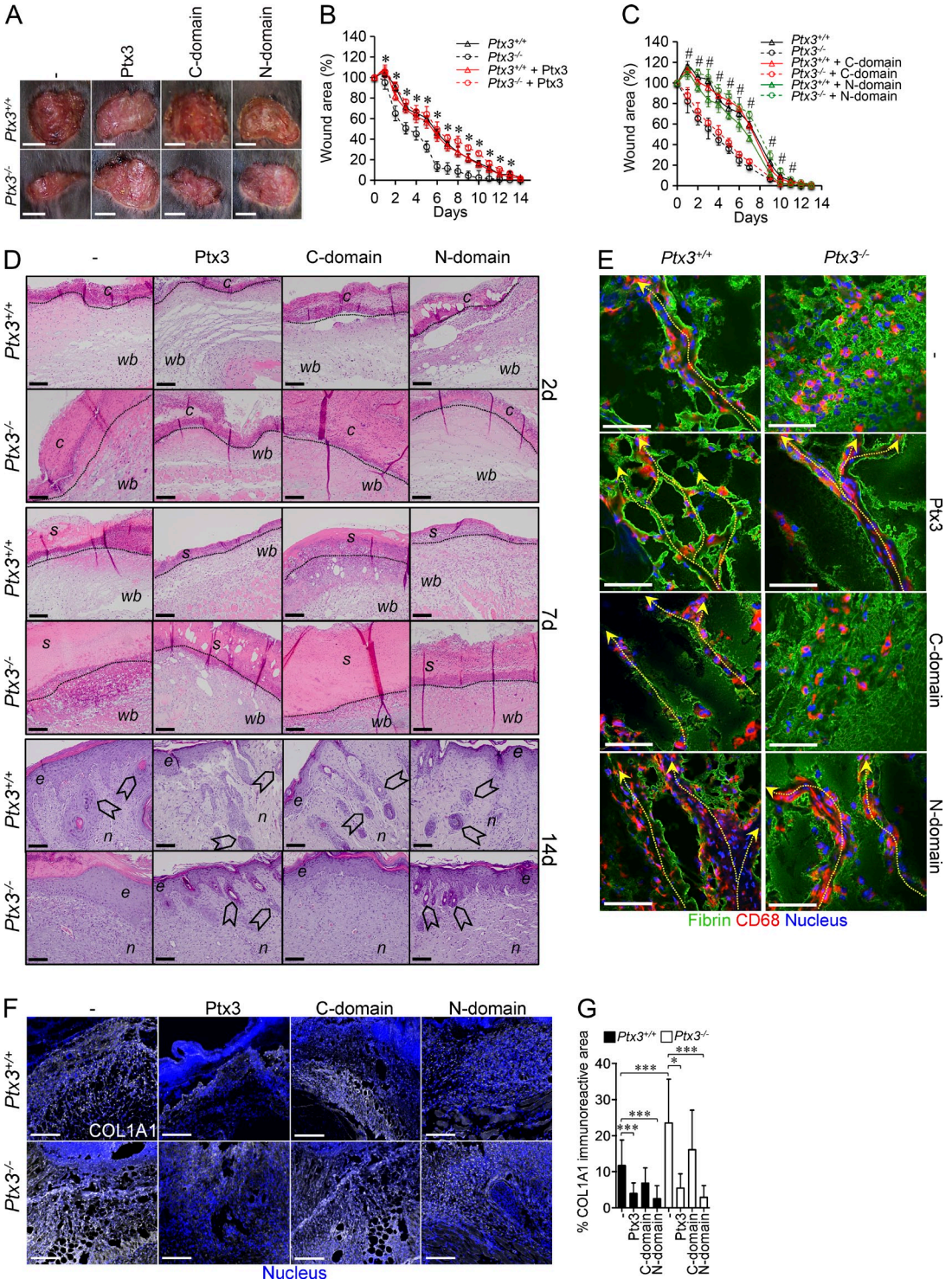

Figure 3. Alterations in skin wounding are rescued by exogenous PTX3. (A–C) After skin wounding in *Ptx3*$^{+/+}$ and *Ptx3*$^{-/-}$ mice, the effect of recombinant PTX3 (A and B) and its N- or C-terminal domains (N or C domain; A and C) on wounded skin area was assessed. (A) Representative macroscopic images of skin wounds were obtained at day 2. Bars, 5 mm. (B and C) Kinetic analysis of skin excisional wound areas was performed. (B) *, $P < 0.01$, *Ptx3*$^{-/-}$ treated with PTX3 versus *Ptx3*$^{-/-}$ (Student's *t* test). One representative experiment ($n = 10–12$ mice/group) out of 2 is shown. (C) #, $P < 0.005$, *Ptx3*$^{-/-}$ treated with the N-domain versus *Ptx3*$^{-/-}$ (Student's *t* test). One representative experiment ($n = 8–10$ mice/group) out of 3 is shown. (D)The effect of treatment with PTX3 and its N- and C-terminal domains on wound healing was evaluated by histological (H&E) staining at the indicated days in WT versus *Ptx3*$^{-/-}$ mice. C, clot; wb, wound bed; s, scab; e, epithelialization; n, neo-formed tissue; arrowheads, hair follicles. Bars: (2 d and 7 d) 100 µm; (14 d) 20 µm. Representative images are shown ($n = 4$ mice). (E) Fibrin deposition and CD68$^+$ invading cells in WT and *Ptx3*$^{-/-}$ wounds after treatment

(Fig. 6, A–C and not depicted). Moreover, skin wound healing was performed in double-deficient *Ptx3*$^{-/-}$ *P-selectin*$^{-/-}$ mice. First P-selectin deficiency had no notable effect on skin healing (Fig. 6 D). Moreover, PTX3/P-selectin double-deficient mice showed a wound healing phenotype identical to that of *Ptx3*$^{-/-}$ mice (Fig. 6 D), suggesting that interaction between PTX3 and P-selectin does not play a major role in the alterations of wound healing observed in PTX3 deficient hosts. Thus, altered P-selectin-dependent leukocyte recruitment is not responsible for the alterations in tissue repair observed in *Ptx3*$^{-/-}$ mice. However, as stated above, in *Ptx3*$^{-/-}$ mice CD68^{+} macrophages and PDGFRα^{+} cells failed to collectively migrate into the fibrin-rich skin wound site.

Interaction of PTX3 with fibrin and plasminogen at acidic pH

The finding that excessive clot and thrombi formation and fibrin deposition and persistence were consistent phenotypes in tissue damage models in *Ptx3*$^{-/-}$ mice and the role of fibrin as a provisional matrix protein guiding subsequent repair (Carmeliet et al., 1994; Bugge et al., 1996; Romer et al., 1996; Singer and Clark, 1999; Schäfer and Werner, 2008) prompted us to investigate the interaction of PTX3 with components of the coagulation and fibrinolytic cascade. We were also prompted in this direction by the finding that PTX3 interacts with ficolins via their fibrinogen domain (Ma et al., 2013). Previous studies indicating that PTX3 induced procoagulant activity in endothelial cells and monocytes (Napoleone et al., 2002) could not be reproduced on repeated attempts (unpublished data). PTX3 bound fibrinogen (FG) and plasminogen (Plg), but it did not bind other components of the coagulation cascade (listed in Materials and methods; unpublished data). When FG, fibrin, and Plg were immobilized on plastic wells, pH-dependent binding was observed, with optimal interaction at pH 5.5–6.5 (Fig. 7 A). In the same setting, C-reactive protein (CRP) did not bind FG, fibrin, or Plg (Fig. 7 B). Binding of PTX3 to fibrin and Plg was Ca^{2+} independent and unaffected by treatment with endoglycosidase F3 or/and neuraminidase (unpublished data). The apparent dissociation constants (K_d) evaluated by nonlinear fitting analysis at pH 6.0 were 31.2 ± 10.5 nM, 7.5 ± 0.9 nM and 66.7 ± 25.1 nM for interaction with FG, fibrin, and Plg, respectively (Fig. 7 C). The N-terminal domain bound FG, fibrin, and Plg, whereas the C-terminal pentraxin domain bound with low-affinity only Plg (Fig. 7 D). The analysis of binding was extended by surface plasmon resonance (Fig. 7, E–G), which showed higher affinity (K_d) of PTX3 or the N-terminal domain for Plg at pH 6.0 than at pH 7.4, due to a faster association rate (K_{on}) at acidic pH. Addition of mAb MNB4, directed against the PTX3 N-terminal domain, completely blocked PTX3 binding to fibrin but not to Plg. mAb MNB5, which recognizes the C-terminal domain, had no effect (Fig. 7 H). Moreover, no competition for binding to PTX3 was observed between fibrin and Plg. Actually, in the presence of PTX3, Plg bound to fibrin more efficiently; similarly, in the presence of Plg, PTX3 bound to fibrin more efficiently (Fig. 7 I). In competition experiments PTX3 binding to Plg was inhibited by L-lysine (Lys; ligand of Lys-binding sites in Plg Kringles [KRs] 1, 2, 3, and 5) and L-arginine (specific ligand of KR5; Law et al., 2012; not depicted). Moreover, PTX3 bound Plg KR3-KR5 fragment, but not KR1-KR3 fragment (Fig. 7 J). These data suggest that PTX3 interacts with Plg KR5, which triggers the Plg conformational change leading to the open form, and does not interact with Plg KR1 domain, which mediates the initial recruitment of closed Plg to the C-terminal Lys moieties of fibrin or cell surface (Law et al., 2012). All together, these data suggest that PTX3 interaction with fibrin and Plg occurred via different sites in the PTX3 N-terminal domain and that interaction of PTX3 with Plg did not interfere with fibrin binding to Plg, and occurred via a different site.

No pH-dependence was observed in the PTX3 interaction with microbes such as *A. fumigatus* conidia, *P. aeruginosa* and *Escherichia coli*, or OmpA from *K. pneumonia* (not depicted).

Functional relevance of PTX3 interaction with fibrin and plasminogen

In an effort to investigate the actual functional relevance of the interaction of PTX3 with FG/fibrin and Plg, an in vitro fibrinolysis assay was used. At pH 6.0 fibrin gel degradation mediated by plasmin and triggered by uPA and tissue plasminogen activator (tPA) was potentiated in the presence of PTX3, which had no activity on its own (Fig. 7 K). No potentiation was instead observed at neutral pH (pH 7.4, not depicted, and 7.6; Fig. 8).

The finding that PTX3 interacted with FG/fibrin and Plg, and facilitated fibrin dissolution at low pH raised the issue of the actual in vivo occurrence and functional relevance of this interaction during wound healing. After skin wounding, colocalization of PTX3 and fibrin and Plg was observed by confocal microscopy in the clot (Fig. 8 A) and in the pericellular matrix of invading cells or associated with Plg^{+} cells at day 2 (Fig. 8 B). Similarly, PTX3 colocalized with fibrin upon liver and lung injury (unpublished data). Treatment with dichloroacetate (DCA) to revert local acidosis inhibited the colocalization between PTX3 and fibrin or Plg, but not between fibrin and Plg (Fig. 8, C and D). Two-photon microscopy was then used to simultaneously measure the pH using a pH-sensitive fluorescent probe (BCECF) and to visualize PTX3 and fibrin and Plg colocalization in the wounded skin area in vivo

with PTX3 and N-terminal and C-terminal domains (day 2) was assessed by immunofluorescence staining. Representative confocal microscopy images are shown (n = 5–7 mice). Dashed arrows shows passages within the fibrin matrix in wound site created by CD68^{+} cells and direction of invasion toward the wound bed. Bars, 10 µm. (F and G) The effect of PTX3 or domain administration on Collagen I (COL1A1) deposition was assessed in the wounds at day 7 by immunofluorescence staining. (F) Bars, 100 µm. Representative confocal microscopy images are shown. G, quantification of COL1A1 deposition is shown from F. Results are mean percentage and SD (n = 2–3 10× images/mouse, 4–9 mice/group). *, P < 0.05; ***, P < 0.005 (Mann-Whitney test).

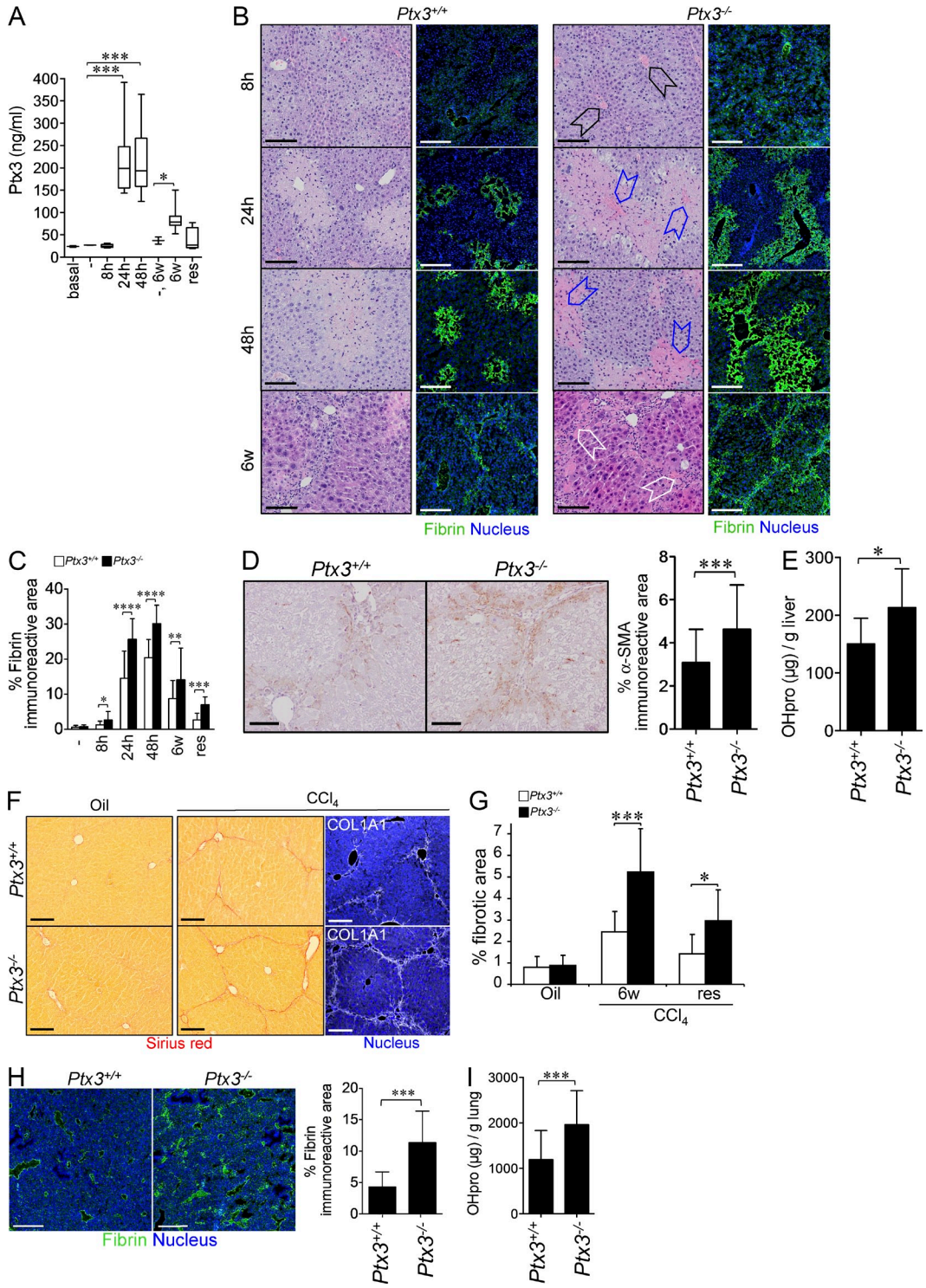

Figure 4. Liver and lung repair is altered in PTX3-deficient mice. Liver and lung injury were induced as described in Materials and methods. (A) PTX3 plasma levels after acute (8-48 h) and chronic (6 wk) CCl_4 treatment, or at resolution of fibrosis were measured. -, treatment with mineral oil as vehicle. Graphs are presented as box plots. *, $P < 0.05$; ***, $P < 0.005$ (Mann-Whitney test); (n = 5–9 independent mice). (B) Representative hematoxylin-eosin and immunofluorescence confocal microscopy images of fibrin in liver sections of WT and *Ptx3*$^{-/-}$ mice are shown. Black arrowheads, centrolobular vein thrombi; blue and white arrowheads, deposits of eosinophilic material-fibrin in necroinflammatory areas (blue) at lobular spaces (24 and 48 h) and in the portal tracts (white) after chronic injury. Bars, 100 μm. (C) Quantification of fibrin staining in the liver was performed on samples from B. Mean ± SD; (B and C) n = 3–8 20× images/mouse, 4–6 mice/group. *, $P < 0.05$; **, $P < 0.005$; ***, $P < 0.001$; ****, $P < 0.0001$ (Mann-Whitney test). (D) Representative immunohistochemistry images for α-SMA (left) and quantification of the immunoreactive areas (right) are shown for WT and *Ptx3*$^{-/-}$ mice. Results are

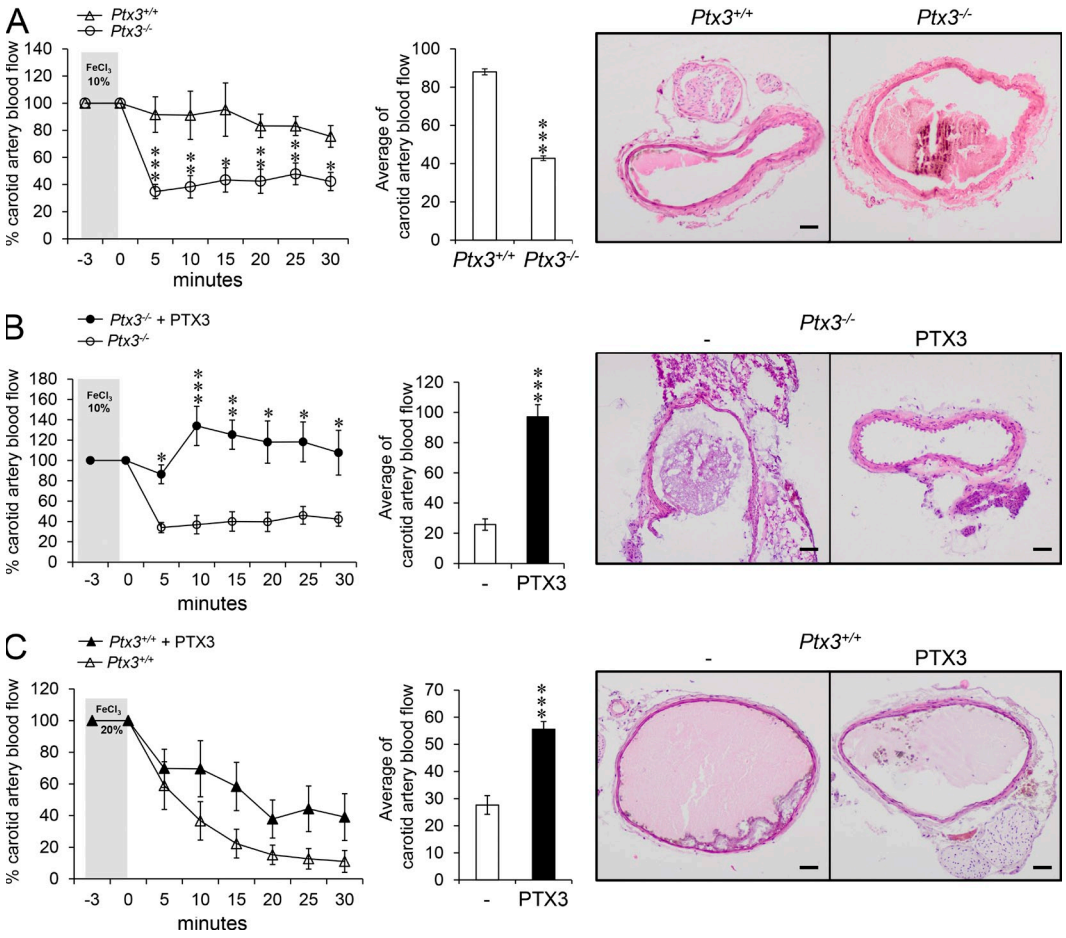

Figure 5. The thrombotic response is increased in PTX3-deficient mice. A model of $FeCl_3$-induced arterial injury was used. (A) Induction of arterial thrombosis in WT and *Ptx3*$^{-/-}$ mice was assessed after topical application of $FeCl_3$ (10%). (B and C) The effects of PTX3 on thrombus formation in *Ptx3*$^{-/-}$ ($FeCl_3$ 10% [B]) and WT ($FeCl_3$ 20% [C]) mice were also assessed. (A–C) Left panel shows carotid artery blood flow expressed as relative percentage compared with the value before injury. Middle panels show the average of carotid artery blood flow measured in the observation period (3–30 min). Results are presented as mean percentage ± SEM. A, (n = 11 WT and 17 *Ptx3*$^{-/-}$ mice); B, (n = 4 WT and 4 *Ptx3*$^{-/-}$ mice); C, (n = 8 WT and 9 *Ptx3*$^{-/-}$ mice). (A–C) *, P < 0.05; **, P < 0.01; ***, P < 0.005 (Student's t test). (A–C, right) Representative histological H&E microscopy images of carotid arterial thrombi. Bars, 100 µm.

(Supplemental material). The surface of the skin normally has an acidic extracellular pH with values ranging from 4.5 to 6, due to the hydrolysis of skin lipids to free fatty acids, whereas lower epidermis and dermis have a neutral-alkaline extracellular pH in the range of 7–9 (Hanson et al., 2002). Accordingly, in the dermis (depth 10–20 µm) of unwounded skin, the pH measured by two-photon microscopy was 7.63 ± 0.5 (mean ± SEM; range 6.53–8.73; mean ± σ). In contrast, in the proximity of the damaged dermis (the analysis of the pH in the wound itself was technically impossible because of the endogenous autofluorescence of the clot) the pH was acidic (6.77 ± 0.5; P = 0.011; range, 5.67–7.87; Fig. 8 E and Fig. S2), which suggests cellular metabolic adaptation to trauma-induced tissue hypoperfusion and hypoxia (Schneider et al., 2007). In the z-projection (14 optical sections of 10 µm) of the dermis between the perilesion area and the wound, a significantly higher colocalization

mean ± SD. ***, P < 0.005 (Student's t test); n = 7–10). 20× images from 4 mice. (E) Collagen deposition in WT and *Ptx3*$^{-/-}$ mice was assessed after chronic injury and measured as liver OH-proline (OHpro) content. (n = 9 WT and n = 10 *Ptx3*$^{-/-}$ independent mice). Results are mean ± SD. *, P < 0.05 (Student's t test). (F) Representative microscopy images for Sirius red and COL1A1 staining in portal septa are shown. Bars, 100 µm. (G) Quantification of liver Sirius red staining at 6 wk and in the resolution phase (res) in WT and *Ptx3*$^{-/-}$ mice after CCl_4 injection from F. Results are presented as the mean percentage fibrotic area ± SD (n = 5–7 mice). *, P < 0.05; ***, P < 0.005 (Student's t test). (H) Fibrin deposition in *Ptx3*$^{-/-}$ and WT lungs was assessed using immunofluorescence staining 7 d after injury. Representative confocal microscopy images are shown (left) and fibrin staining quantification is presented (right). Bars, 100 µm. Mean ± SD; n = 3–5 10× images/mouse, 3 mice/group. ***, P < 0.0001 (Mann-Whitney test). (I) OH-proline (OHpro) content was measured in *Ptx3*$^{-/-}$ and WT lungs, 30 d after injury. ***, P < 0.005 (Student's t test). n = 17 WT and 29 *Ptx3*$^{-/-}$ independent mice.

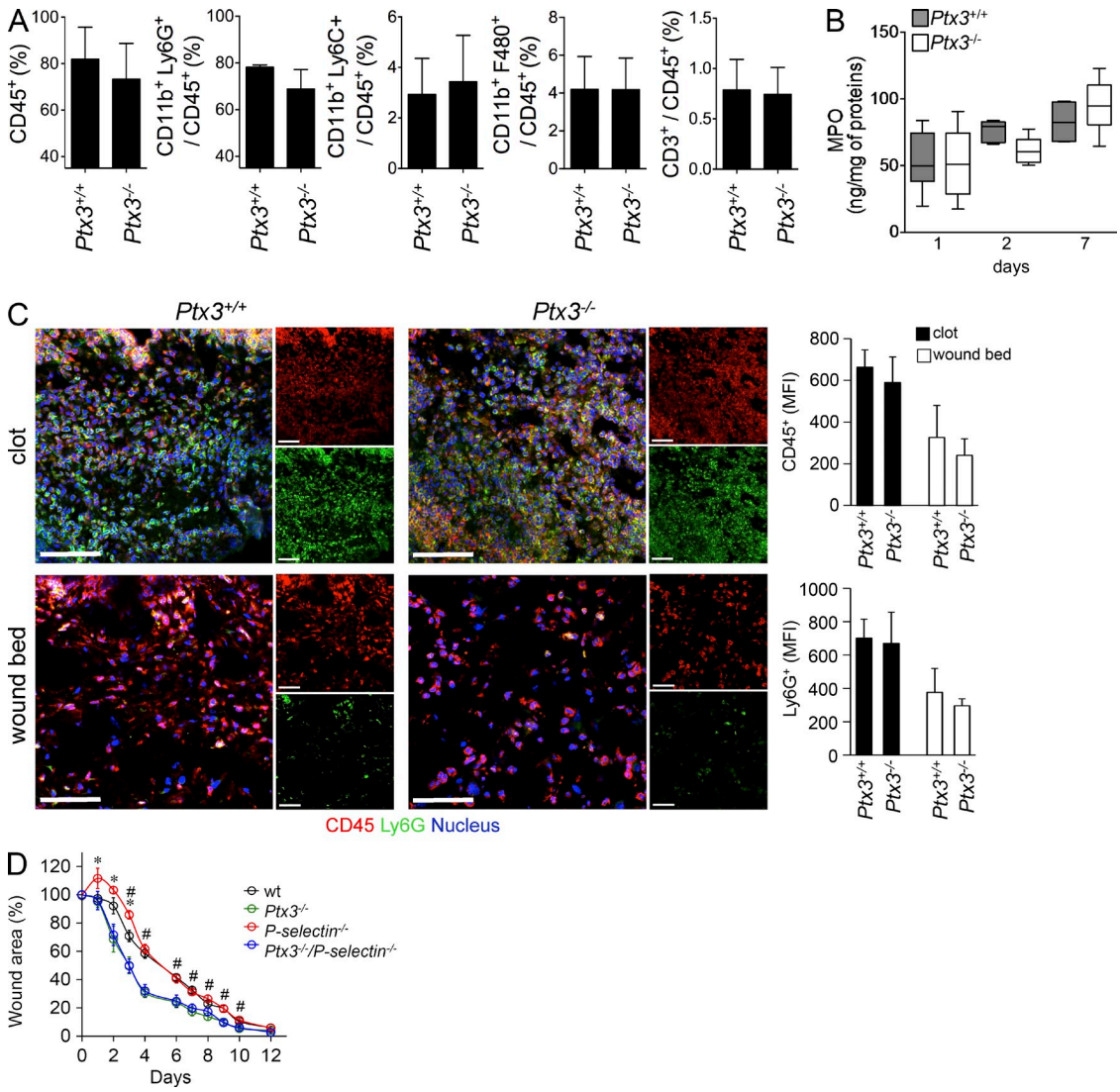

Figure 6. Total leukocyte infiltration was not impaired in *Ptx3*$^{-/-}$ skin wound. Skin wounding was performed. (A) An analysis of leukocytes infiltrating the wound site (day 1) by cell flow cytometry was performed for *Ptx3*$^{+/+}$ and *Ptx3*$^{-/-}$ mice. Quantification histograms are shown for the indicated cell populations. Results are presented as mean percentage ± SD; $n = 4$ independent mice each. (B) MPO content was measured in the course of wound healing at days 1, 2, 7. $n = 8$–10, day 1; $n = 10$ and 11, day 2; $n = 6$ and 8, day 7, WT and *Ptx3*$^{-/-}$ independent mice, respectively. (C) Representative immunofluorescence confocal microscopy images of CD45$^+$ and Ly6G$^+$ staining in the clot and damaged dermis 2 d after injury are shown. (left) Merged or single confocal images are shown (CD45, red; Ly6G, green; nucleus, blue). Bars, 50 µm. (right) MFI quantification in the entire field of view is shown. Data are presented as mean ± SD; ($n = 5$–7 mice; 4–12 images per mouse were analyzed). (D) A kinetic analysis of skin excisional wound areas in WT, *Ptx3*-, *P-selectin*-, and *P-selectin–Ptx3*-deficient mice was performed. Values represent mean ± SEM of one representative experiment out of two ($n = 7$–9 mice/group). #, $P < 0.05$, *P-selectin*$^{-/-}$/*Ptx3*$^{-/-}$ compared with *P-selectin* $^{-/-}$ mice and *, $P < 0.05$, *P-selectin* $^{-/-}$ compared with WT (Student's *t* test).

of PTX3 and plasminogen was measured in a representative lower pH region than in a representative higher pH region (Fig. 8, F and G) of the wound site, with Pearson's coefficients of 0.28 ± 0.03 and 0.15 ± 0.03, respectively ($P = 0.007$). Similarly, a significantly higher colocalization of PTX3 and fibrin was observed in the lower pH area (Pearson's coefficients: 0.83 ± 0.05 and 0.63 ± 0.07 in lower pH and higher pH regions, respectively, $P = 0.005$). Binding of PTX3 to fibrin and Plg (Fig. 8 H), and amplification of cell free fibrinolytic activity by PTX3 (Fig. 8, I and J) were confirmed at the mean pH measured by two-photon microscopy in wounded skin (pH 6.77).

Moreover, PTX3-deficient wounds showed decreased Plg deposition and plasmin formation (Fig. 9, A and B), and lower levels of D-dimer compared with WT lesions at day 2 after wounding (Fig. 9 C).

Macrophages are key players in tissue repair, orchestrate pericellular fibrinolysis in vitro and in vivo (Carmeliet et al., 1994; Cook et al., 2006), and are major sources of PTX3 (Martinez et al., 2009). Because of these factors, and in light of the defective invasive phenotype of macrophages observed in *Ptx3*$^{-/-}$ mice (Fig. 2 D), we assessed pericellular fibrinolysis mediated by *Ptx3*$^{-/-}$ macrophages. As shown in Fig. 9 D, *Ptx3*$^{-/-}$

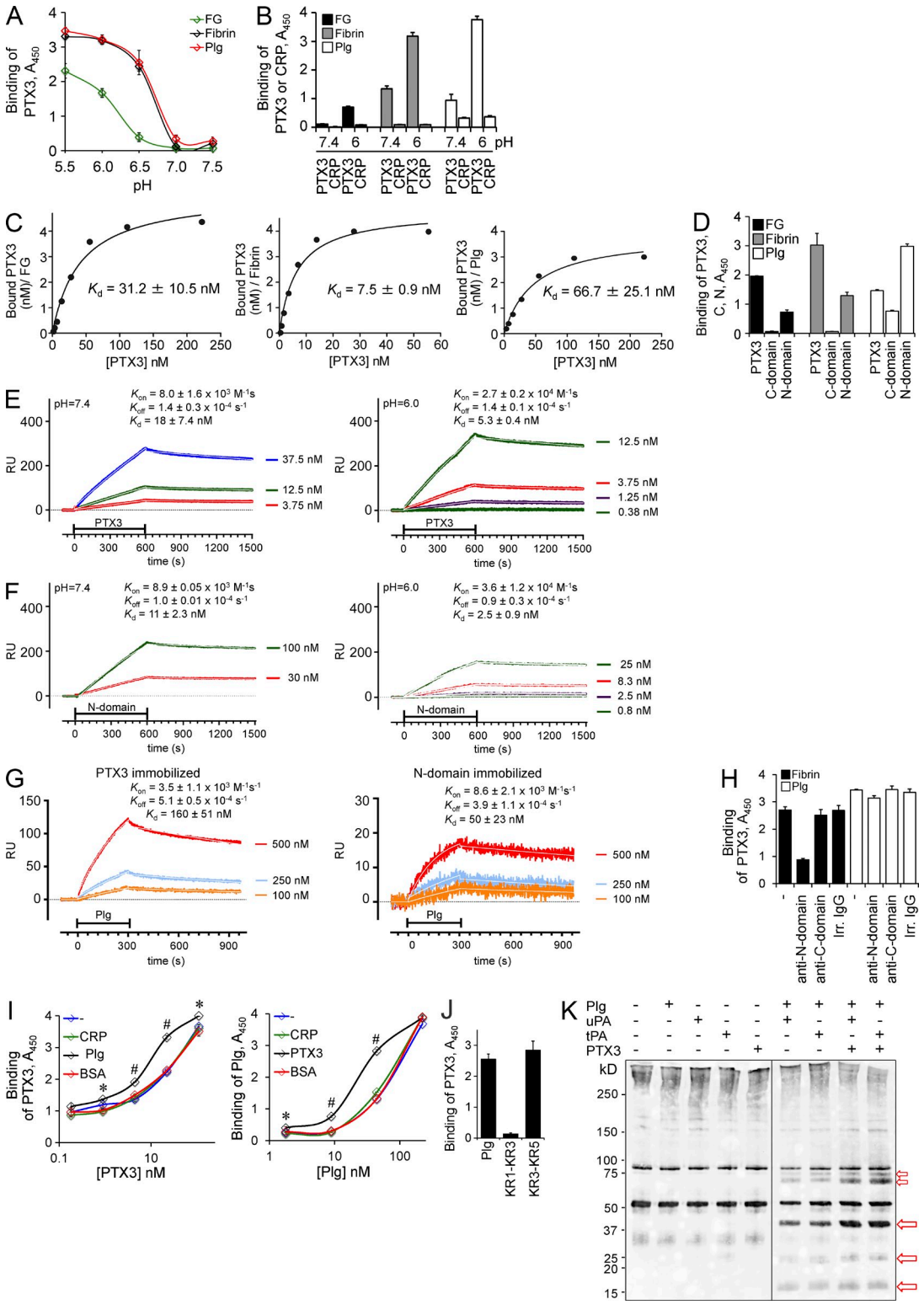

Figure 7. PTX3 interacts with fibrinogen, fibrin, and plasminogen. (A–D) A microtiter binding assay was performed to assess the interaction between PTX3 or CRP to fibrinogen (FG), fibrin, and plasminogen (Plg) in vitro. (A) The binding of PTX3 (22 nM) to FG, fibrin, and Plg at different pHs was assessed. Results are expressed as mean ± SD. One representative experiment in triplicate out of 5 is shown. (B) The binding of PTX3 and CRP to FG, fibrin, and Plg at pH 7.4 or 6.0 was also assessed. One representative experiment in triplicate out of three is shown. (C) Fitting analysis of biotinylated (b-) PTX3-FG–fibrin–Plg interactions. Mean values of 6 (FG and Fibrin) or 3 (Plg) experiments are shown. (D) Binding of b-PTX3 and b-C-terminal or b-N-terminal domains (4.4 nM) to FG, fibrin, Plg at pH 6.0 was assessed. One representative experiment in triplicate out of seven is shown. (E–G) Surface plasmon

peritoneal macrophages showed defective fibrinolytic activity compared with WT cells. Similar results were obtained with PTX3-deficient and -sufficient embryonic fibroblasts (Fig. 9, E and F).

In an effort to assess whether an interaction with key components of the coagulation/fibrinolysis system actually underlies the role of PTX3 in wound healing, pharmacologic inhibitors of fibrin deposition with different molecular targets were used. These included antithrombin III (ATIII; an inhibitor of thrombin and Factor Xa), Argatroban (thrombin inhibitor), and Batroxobin (which depletes fibrinogen). In the presence of these inhibitors of the coagulation cascade, the differences in skin wound healing (accelerated reduction of wound area and collagen accumulation) between PTX3-competent and -incompetent mice were abolished (Fig. 10, A–F).

DISCUSSION

The results reported here show that a prototypic component of humoral innate immunity, the long pentraxin PTX3, plays a nonredundant role in the orchestration of tissue repair and remodeling. In different models of tissue damage, PTX3 deficiency was associated with increased fibrin deposition and persistence, followed by increased collagen deposition. In addition, after injury, PTX3 interacted with FG/fibrin and Plg at acidic pH and, based on in vitro findings, this tripartite interaction promoted fibrin degradation, which is a premise for appropriate repair.

Major defects in skin wound healing in PTX3-deficient mice included increased clotting, excessive fibrin accumulation, and delayed reepithelialization at early time points, followed by augmented collagen deposition, epithelial hyperplasia, and defective mature tissue formation at healing. Delayed reepithelialization followed by epithelial hyperplasia are signs of defective repair, which have been associated to impaired degradation of the extracellular matrix by leading edge keratinocytes and excessive keratinocyte proliferation, respectively (Lund et al., 2006). In two other models studied (liver and lung injury), we observed that tissue damage was associated with increased fibrin deposition and collagen content. Results presented here on the interaction of PTX3 with fibrin and plasminogen suggest that defective pericellular fibrinolysis of remodeling cells associated to PTX3 deficiency is responsible for these defects. Along the same line, in arterial thrombosis, PTX3 deficiency was associated to increased thrombus formation and reduced blood flow. Collectively, these data indicate that PTX3 plays an essential role in the orchestration of a tissue injury response, in agreement with previous studies (Salio et al., 2008; Norata et al., 2009; Deban et al., 2010; Rodriguez-Grande et al., 2014).

In the skin wound model, which was more deeply investigated, the major sources of PTX3 throughout the course of healing were stromal cells of mesenchymal origin, whereas neutrophils and macrophages contributed in the early phase. TLR and IL-1 are key activators of the inflammatory and reparative responses in tissue injury and potent inducers of PTX3 (Medzhitov, 2008; Dinarello, 2009; Bottazzi et al., 2010). Results obtained with mice deficient of components of the TLR or IL-1 signaling pathway (IL-1R, MyD88, and TRIF) indicate that after tissue damage, the induction of PTX3 was downstream of TLR sensing and IL-1 amplification and required both MyD88- and TRIF-dependent signaling pathways. However, we cannot exclude that the low content of PTX3 in wounded skin of mice deficient of TLR or IL-1 signaling components was also caused by defective recruitment of inflammatory cells at the wound site, as reported for TLR3-deficient mice (Lin et al., 2011).

PTX3 binds P-selectin via its glycosidic moiety and negatively regulates leukocyte recruitment in P-selectin–dependent models of inflammation (Deban et al., 2010; Lech et al., 2013). The role of individual selectins in leukocyte recruitment and tissue repair in models of wound healing has been the object of conflicting reports (Subramaniam et al., 1997; Yukami et al., 2007; Tomita et al., 2009). In an effort to assess whether the role of PTX3 in the orchestration of wound healing was dependent on its interaction with P-selectin, double deficient mice were used. We found that the alterations in wound healing were identical in $Ptx3^{-/-}$ and $Ptx3^{-/-}$ /*P-selectin*$^{-/-}$ mice. Thus, the role of PTX3 in the orchestration of tissue repair in skin wound healing is P-selectin independent.

It has been previously demonstrated that recombinant PTX3 at supraphysiological concentrations (10–40 μg/ml) interferes with platelet aggregation induced by thrombin receptor agonist peptide-6 (TRAP) and collagen (Maugeri et al., 2011). However, results obtained with gene-targeted mice indicated that PTX3 deficiency does not impact on platelet aggregation (unpublished data). This suggests that at physiological concentration PTX3 is not involved in this process and that the phenotypes described here do not depend on increased platelet aggregation.

resonance (SPR) sensorgrams were obtained by injecting different concentrations of PTX3 (E) or PTX3 N-terminal domain (F) over immobilized Plg. (G) SPR analysis was performed at pH 6.0 flowing monomeric Plg onto immobilized PTX3 or N-terminal domain. (E–G) One representative experiment out of two is shown. (H–J) Microtiter binding assays were performed to define which PTX3 domain and plasminogen fragment are involved in the interaction. (H) PTX3 binding to fibrin and Plg in the presence of antibodies anti–N-terminal (MNB4) or anti–C-terminal (MNB5) domains or irrelevant IgG was assessed as shown. One representative experiment in triplicate out of three is shown. (I) The binding of PTX3 (top) or Plg (bottom) to fibrin in the presence of Plg or PTX3, respectively, and of CRP and BSA used as controls, at pH 6.0 was assessed as shown. One representative experiment in triplicate out of two is shown. *, $P < 0.05$; #, $P < 0.001$. Values are mean ± SD. (J) The binding of PTX3 to Plg fragments, at pH 6.0 was assessed as shown. One representative experiment in triplicate out of 4 is shown. (K) Western blot analysis of fibrin clots prepared by mixing FG and thrombin, digested at pH 6.0 by recombinant purified proteins in cell-free conditions, was performed. Red arrows indicate the presence of main products of fibrinolysis. One representative experiment out of five is shown.

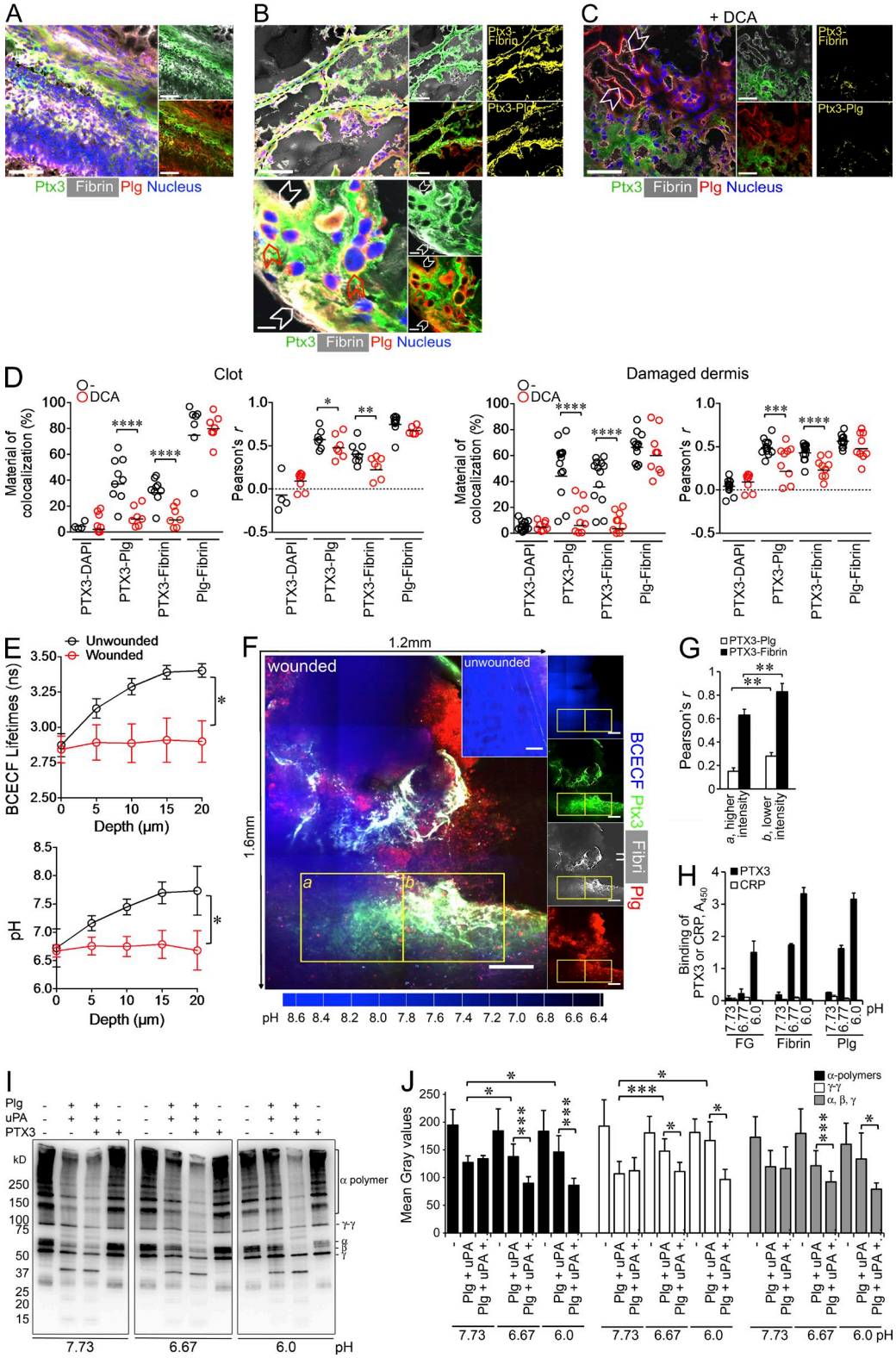

Figure 8. The interaction of PTX3 with fibrin and plasminogen occurs in vivo. Skin wounding was performed in untreated WT mice (A and B) or upon treatment with DCA (C). (A–C) Colocalization of PTX3, fibrin, and Plg in clot (A) and damaged dermis (B and C) of wounded skin at day 2 were assessed. (A–C, left) Representative immunofluorescence confocal microscopy merged images of PTX3 (green), fibrin (white), Plg (red), and nucleus (blue). (A, right; B and C, middle) Representative merged images of PTX3 (green) and fibrin (white), or of PTX3 (green) and Plg (red). (B and C, right) Images of colocalization signal (yellow) of PTX3 with fibrin (PTX3-Fibrin) or plasminogen (PTX3-Plg). (B, top) Passages created by invading cells within

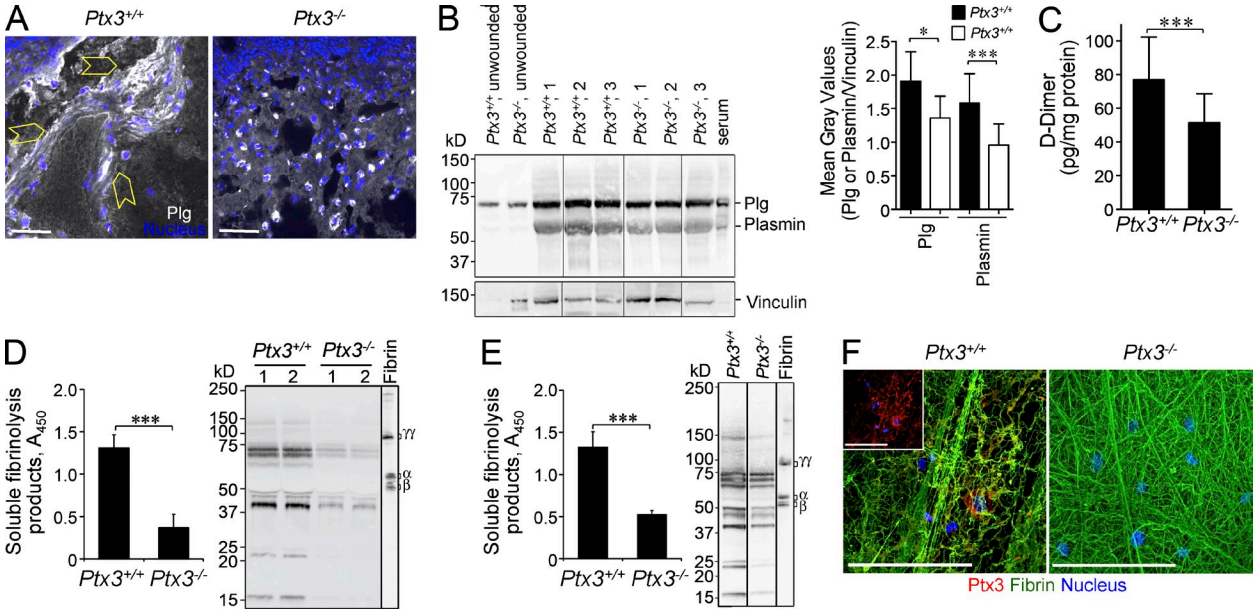

Figure 9. The interaction of PTX3 with fibrin and plasminogen is functionally relevant. Skin wounding was performed in *Ptx3*$^{+/+}$ and *Ptx3*$^{-/-}$ mice. Representative confocal microscopy images (A) and Western blot analysis (B) of Plg/plasmin (white) at day 2 after skin wounding are shown. (A) Plg/plasmin (white) and cells invading the wound bed (yellow arrowheads) are shown. Bars, 20 µm. (n = 2–5 40X images/mouse, 4 mice/group). (B) one representative experiment out of 3 with 50 µg/lane of wound protein extract from 3 mice per genotype and 1 µl/lane of mouse serum is shown. Vinculin immunoblotting (loading control) is also shown. Results are expressed as mean ± SD gray intensity values of Plg or plasmin/vinculin. (n = 6 mice/group). (C) An ELISA of D-dimer in skin wound extracts on day 2 was performed. (n = 16 WT and 17 *Ptx3*$^{-/-}$ independent mice). (D and E) An ELISA (left) and a Western blot analysis (right) of soluble fibrinolysis products generated by WT or *Ptx3*$^{-/-}$ peritoneal macrophages in (D) or embryonic fibroblasts (MEFs) in (E) grown in fibrin clots as described in Materials and methods in 3 and 2 d of culture, respectively, are shown. (D) (left) Data are presented as mean ± SD of one representative experiment in triplicate with 2–3 independent mice out of 4; (right) one experiment of 2 performed is shown. (F) Representative confocal microscopy images of WT or *Ptx3*$^{-/-}$ MEF after 2 d of culture in a fibrin matrix, to assess remodeling of the matrix, as well as apparent colocalization of PTX3 and fibrin fibers in WT versus *Ptx3*$^{-/-}$ cultures. (inset) PTX3 staining (red) and nucleus (blue) are shown. Bars, 50 µm. (E and F) One representative experiment with three independent mice out of two is shown. (C–E) ***, P < 0.005 (Student's t test).

Fibrin and other provisional ECM proteins are transiently deposited after tissue injury and their subsequent degradation heralds tissue remodeling and scar formation. Genetic evidence points to an essential role of timely fibrin deposition in tissue repair in different models, including skin wound healing and liver and lung injury (Carmeliet et al., 1994; Romer et al., 1996; Pohl et al., 2001; Idell, 2003; de Giorgio-Miller et al., 2005; Calvaruso et al., 2008). Thus, PTX3 acts as a molecular scaffold

fibrin rich-wound sites (dashed black arrows); (bottom) magnification image of PTX3 colocalization with fibrin and Plg at the pericellular matrix of cells invading the wound bed (white arrowheads) and with Plg^{+} invading cells (red arrowheads). Bars: (A, B [top], and C) 50 µm and (B, bottom) 5 µm. (C) The inhibition of colocalization after treatment with DCA was assessed 2 d after wounding. Representative confocal microscopy images are shown. White arrowheads denote colocalization between Plg and fibrin matrix. (A–C) n = 4–9 images/mouse, 4 mice/group. (D) Colocalization in the clot (left) and in the damaged dermis (right) of wounded skins (day 2) was quantified upon treatment with DCA (from samples in A–C and not depicted). The percentage of colocalized PTX3 with fibrin or plasminogen, and fibrin with plasminogen (top), and the relative Pearson's coefficient (bottom) are shown. Each circle represents analysis from a single confocal image (2–3 fields of vision/mouse, n = 3–4 mice). *, P < 0.05; **, P < 0.01; ***, P < 0.005; ****, P < 0.0005; (Mann-Whitney test). (E) Measurement of pH in the skin was assessed by two-photon microscopy in unwounded skin and at the periphery of the wound. The data represent mean ± SEM. BCECF lifetime and pH as a function of depth. (n = 5 mice/group). *, P < 0.05 (Student's t test). (F) Representative two-photon microscopy images from D are shown. A tiling presentation of images showing the colocalization of PTX3, fibrin and Plg in areas of acidic pH (blue, lower intensity) at the wound site is presented (left). Inset, unwounded skin, control. Single fluorescence images are presented (right). Images are composite maximum intensity projections in the proximity of damaged dermis. Bars, 200 µm. Representative images from one mouse out of 10 WT mice analyzed are shown. (G) Colocalization analysis (Pearson's coefficient) was measured for PTX3-Plg and PTX3-fibrin in insets *a* (blue higher intensity, higher pH) and *b* (blue lower intensity, lower pH) of panel F of PTX3 with fibrin or plasminogen. Data are presented as mean ± SD of 14 slices (10 µm) in the z axis. (H) The binding of PTX3 (22 nM) and CRP (22 nM) to FG, fibrin, and Plg was assessed at pH 7.73, 6.7,7 and 6.0 by microtiter binding assay. Data are presented as mean ± SD of one representative experiment in triplicate out of 2. (I and J) Western blot analysis (I) and quantification (J) of fibrin clots digested at pH 7.73, 6.77, and 6.0 by recombinant purified proteins in cell-free conditions was performed. I, On the right, α polymers, γ dimers and α, β, and γ subunits are shown. One representative experiment out of four is shown. (J) Results are expressed as mean ± SD. Gray intensity values in bands of α polymers, γ dimers and α, β, and γ subunits from four Western blots performed are shown.

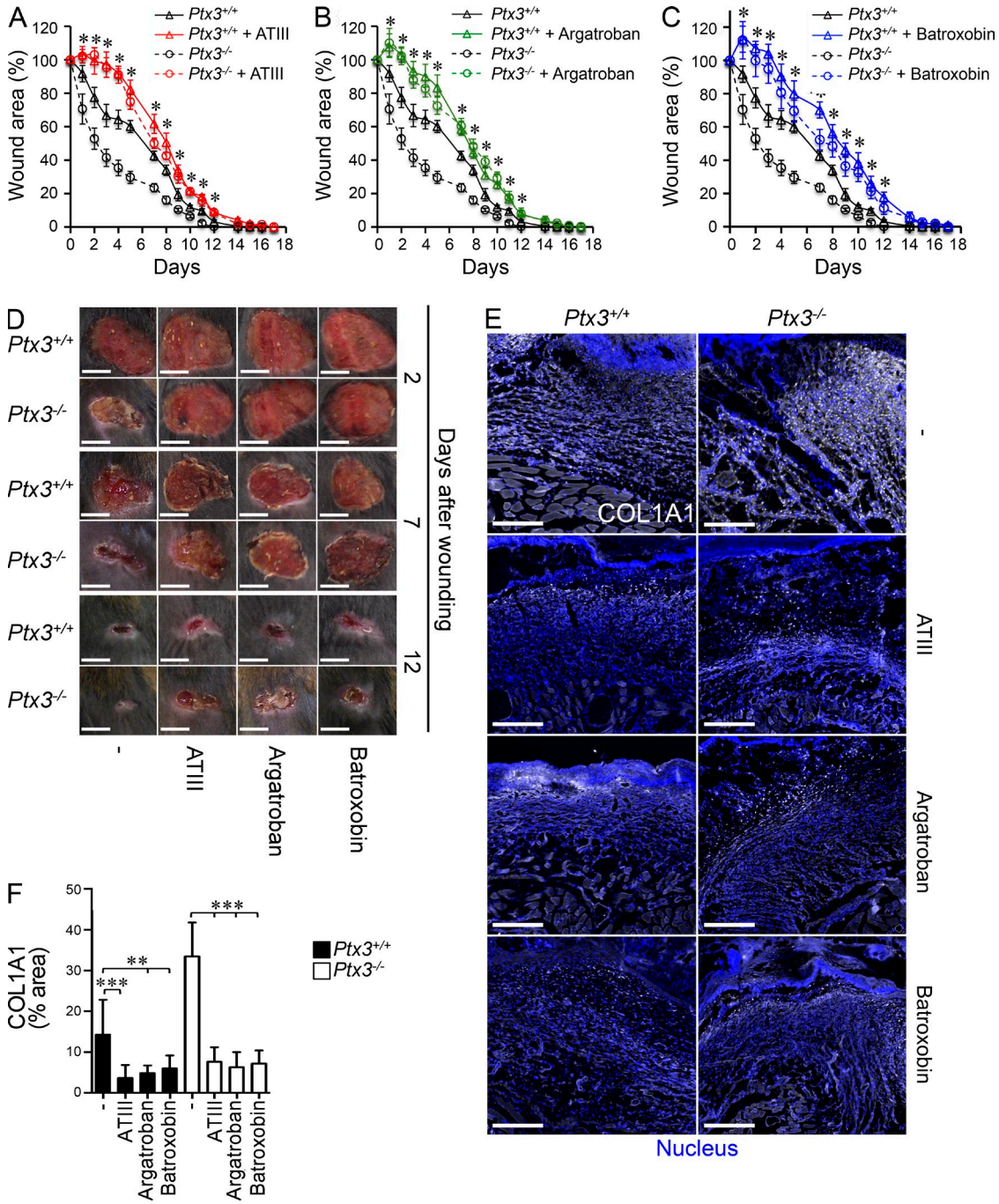

Figure 10. Inhibitors of coagulation and fibrin deposition rescue the phenotype of *Ptx3*$^{-/-}$ mice in skin wound healing. (A–C) A kinetic analysis of skin excisional wound areas after treatment with ATIII (A), Argatroban (B), and Batroxobin (C) was performed in WT and *Ptx3*$^{-/-}$ mice; *, $P < 0.005$, *Ptx3*$^{-/-}$ treated versus *Ptx3*$^{-/-}$ (Student's *t* test). One representative experiment with 8–10 mice/group out of 2 is shown. (D) Representative macroscopic images of WT and *Ptx3*$^{-/-}$ skin wounds after treatment with ATIII, Argatroban, and Batroxobin at the indicated days after wounding are shown. (E and F) Representative confocal microscopy images (E) and quantification (F) of COL1A1 deposition in wounded skin (on day 7) after treatment with the indicated pharmacological agents in WT and *Ptx3*$^{-/-}$ mice from A–C are shown. (E) Bars, 100 µm. (E and F) Results are presented as mean percentage of area ± SD (n = 5–8 images from 4 mice/experimental group). **, $P < 0.01$; ***, $P < 0.005$ (Mann-Whitney test).

favoring the interaction of Plg with fibrin and its timely degradation as a premise for appropriate repair. This activity is peculiar for PTX3 because short pentraxins did not show binding to fibrin, fibrinogen, or plasminogen. Accordingly, the second exon-encoded N-terminal domain of PTX3 recapitulated the activity of the whole molecule both in vitro and in vivo.

The interaction of PTX3 with FG/fibrin and Plg was much more efficient (from three- to fourfold) at acidic pH. An acidic

pH ranging from 5.5 to 6.9 occurs at sites of tissue injury (Schneider et al., 2007) and in growing tumors (Gatenby and Gillies, 2004). The Plg activators uPA and tPA are neutral proteases (Hamilton, 1980) and accordingly, we observed that cell-free fibrinolysis was less effective at acidic pH compared with neutral pH. The presence of PTX3 in the assay increased fibrinolysis efficiency at acidic pH. Thus, the pH dependence of the binding of PTX3 to FG/fibrin and Plg ensures that it does not occur in the circulation but rather at sites of tissue repair, where it sustains fibrin matrix resolution in an acidic environment.

PTX3 is an essential component of humoral innate immunity that interacts with microbial moieties, activates and regulates the complement cascade and has opsonic activity via Fcγ receptors (Garlanda et al., 2002; Lu et al., 2008; Bottazzi et al., 2010; Cunha et al., 2014). The results reported here suggest that, by interacting with the provisional matrix protein fibrin, PTX3 contributes to the orchestration of tissue repair and remodeling. The acidic pH, which occurs during tissue injury and repair (Schneider et al., 2007), is likely to act as a switch on signal for this function of PTX3.

Thus, an essential component of humoral innate immunity has dual functions related to microbial and matrix recognition. Matrix components such as fibronectin (Proctor, 1987), mindin (He et al., 2004), vitronectin (Gerold et al., 2008), and osteopontin (Schack et al., 2009) have opsonic activity for certain microbial species. Molecular phylogenetic analysis suggests that the ancestral function of fibrinogen-domain containing proteins is defense (Hanington and Zhang, 2011). Recent data highlight the connection and interplay between hemostasis and immunity (Semple et al., 2011; Wong et al., 2013). Fluid-phase PRM, such as complement defense collagens (C1q and collectins; Groeneveld et al., 2005), SAP (Dyck et al., 1980), and CRP (Suresh et al., 2004), interact with ECM components. Thus, recognition of both matrix and microbial components is a recurrent theme in the humoral arm of the innate immune system. We suggest that recognition of microbial moieties and ECM components are evolutionarily linked and represent complementary, ancestral properties of humoral innate immunity.

MATERIALS AND METHODS

Reagents

The following reagents were used: pyrogen-free saline (S. A. L.; Bergamo); RPMI 1640 medium (Biochrom); 200 mM l-glutamine (Biochrom); aseptically collected FCS (Hyclone Laboratories); thrombin and recombinant urokinase-type Plg activator (uPA; R&D Systems); human plasma Plg-depleted FG, Glu-Plg, tissue Plg activator (tPA), and CRP (EMD Millipore); Cascade Blue trisodium salt and 2′,7′-Bis-(2-Carboxyethyl)-5-(and-6)-carboxyfluorescein (BCECF free acid; Invitrogen); Coumarin 314 (Sigma-Aldrich); plasma antithrombin III and Argatroban monohydrate (Sigma-Aldrich); Batroxobin (Pentapharm); recombinant Plg fragments KR1-KR3 (#ab73645; AbCam) and KR3-KR5 (#P00747; Gln274~Cys560; USCN Life Science Inc.); Factor II/Thrombin, Factor III, Factor VII, Factor XIV, αVβ3, and PAI-1 (R&D Systems); and recombinant human Annexin II (AbD Serotec). Recombinant human and mouse PTX3, and the PTX3 C-terminal (C domain) and N-terminal (N domain) fragments were purified under endotoxin-free conditions by immunoaffinity, ion-exchange chromatography, and gel filtration, respectively, from the supernatants of stably transfected CHO cells as previously described (Bottazzi et al., 1997; Deban et al., 2010). Purified OmpA from *Klebsiella pneumonia* was prepared as previously described (Jeannin et al., 2005). Rabbit polyclonal antibody to PTX3 and rat monoclonal antibodies anti-PTX3 MNB4 (IgG2a) and MNB5 (IgG1) were obtained as previously described (Camozzi et al., 2006). The rat isotype control was from AbCam (IgG1; #RTK2071). All proteins were at least 95% pure as assessed by SDS-PAGE followed by silver staining.

Animals

PTX3-deficient mice were generated as previously described (Garlanda et al., 2002) and were used on a 129/SvPas or C57BL/6J inbred (backcrossed for 11 generations) genetic background. Wild-type mice were obtained from Charles River or were cohoused littermates (e.g., 2 out of 15 experiments for skin wound healing). *Il1r1*$^{-/-}$, *P-selectin*$^{-/-}$, *Tlr3*$^{-/-}$, and *Ticam1*$^{-/-}$ (all on a C57BL/6J genetic background) mice were from The Jackson Laboratory. *Irf3*$^{-/-}$ and *Myd88*$^{-/-}$ mice were provided by K.A. Fitzgerald (University of Massachusetts Medical School, Worcester, MA) and S. Akira (Osaka University, Osaka, Japan), respectively. *Ptx3/P-selectin*-double-deficient mice were generated by crossing single-deficient mice. Mice were housed in the specific pathogen–free animal facility of the Humanitas Clinical and Research Center in individually ventilated cages and were used between 8 and 12 wk of age. Procedures involving animals handling and care were conformed to protocols approved by the Humanitas Clinical and Research Center (Rozzano, Milan, Italy) in compliance with national (4D.L. N.116, G.U., suppl. 40, 18–2-1992; D.L. N. 26, G.U. 4–3-2014) and international law and policies (EEC Council Directive 2010/63/EU, OJ L 276/33, 22–09-2010; National Institutes of Health Guide for the Care and Use of Laboratory Animals, US National Research Council, 2011). The study was approved by the Italian Ministry of Health (approval n. 71/2012-B, issued on the 09/03/2012). All efforts were made to minimize the number of animals used and their suffering.

Animal models

Skin wound healing. A punch wound was generated on the back of each mouse as previously described (Nakayama et al., 2010). In brief, the hair on the backs of mice (129/Sv or C57BL/6J) was shaved and exposed skin was cleaned with 70% ethanol. A full-thickness wound was created with disposable 8-mm-diam biopsy punch by excising the skin and the underlying panniculus carnosus. Gentamicin was immediately applied and upon histological analysis no gross infection was apparent through day 14. Wound sites of each mouse were digitally photographed and measured every day in the course of wound healing. The edges of the wounds were daily traced onto a transparency, and the areas of open wounds were calculated using ImageJ software (National Institutes of Health [NIH]; Nakayama et al., 2010). Changes of wound area over time were expressed as percentage of the initial wound areas. To study the effect of recombinant PTX3 and its domains on wound healing, 50 µl/20 g body weight of PTX3 (50 µg/ml) and C and N domain (100 µg/ml) or PBS^{2+} were administered i.p. 4 h before injury, and then daily s.c. in the perilesion area. Rescue experiments were performed by treating WT and PTX3-deficient mice with antithrombin III (thrombin and Factor Xa inhibitor; 100 U/kg), Argatroban (thrombin inhibitor; 30 mg/kg), Batroxobin (FG depleting agent; 30 BU/kg), and sodium dichloroacetate (DCA, pH 7.4, inhibitor of lactic acidosis; 300 mg/kg) or vehicle, i.p. 4 h before injury and daily. Each treatment with Batroxobin caused FG depletion for 16-24 h. At indicated time points, mice were anesthetized by i.p. injection of 2.5% Avertin (Tribromoethanol; Sigma-Aldrich), and blood was collected from the inferior vena cava. Skin biopsy specimens were obtained 2 and 7 d after wounding, and at healing (day 14) after cutting of wounds and surrounding areas with 8-mm-diam biopsy punches, and then extensively washed in ice-cold PBS^{2+}, fixed with 4% paraformaldehyde, and embedded in paraffin or dehydrated with a sucrose gradient and embedded in OCT compound (Diapath) and stored at −80°C, for histology studies or confocal microscopy analysis, respectively.

Liver injury. Mice (129/Sv) were injected s.c. with 50 µl/20 g of carbon tetrachloride (CCl_4) dissolved in a 1:1 ratio with mineral oil (Sigma-Aldrich), as

previously described (Mitchell et al., 2009). For acute studies, animals were injected once with CCl_4 and euthanized after 8, 24, and 48 h. For chronic studies, animals were treated twice a week for 6 wk and sacrificed 2 and 10 d after the last CCl_4 injection, respectively, for fibrosis and fibrosis resolution quantification. Livers were then perfused by flushing 5 ml PBS^{2+}, excised, and embedded in paraffin for histological analysis or frozen in OCT compound at −80°C for confocal microscopy analysis.

Lung injury. Acid-induced acute lung injury was performed as previously described (Deban et al., 2010). Lungs were sampled to analyze fibrin deposition and collagen content, 1 and 4 weeks after damage, respectively.

Arterial thrombosis. Experimental arterial thrombosis was induced as previously described (Barbieri et al., 2012). In brief, mice (8–12 wk old, C57BL/6J) were anesthetized with ketamine chlorydrate (75 mg/kg) and medetomidine (1 mg/kg;Virbic). The left carotid artery was dissected free and placed in the probe (model 0.7V; Transonic System) connected to transonic flow meter (Transonic T106). After blood flow stabilization (baseline flow constant for 7 min), filter paper imbibed with $FeCl_3$ (10-20%) was applied downstream of the probe to the top of the exposed carotid. After 3 minutes, the filter paper was removed, the carotid artery was washed with PBS, and the flow was recorded for 30 minutes.

RNA and protein

Real-time PCR experiments were performed using the SybrGreen PCR Master Mix (Applied Biosystems) in a 7900HT fast real-time PCRsystem (Applied Biosystems) in accordance to the manufacturer's instructions (Applied Biosystems) and the following primers: *Ptx3*, 5′-ATTGCTGTTTCACAACCTGC-3′, 5′-CGCTGTGCTGGAGGAACT-3′; or 5′-ACGAAATAGACAATGGACTTC-3′, 5′-AGTCGCATGGCGTGGG-3′ (for sorted cells); *TF*, 5′-CCGACGAGATTGTGAAGGATGT-3′, 5′-AGAGGCTCCCCAGCAGAAC-3′. Data were normalized by *β-actin* or GAPDH expression, analyzed with the Δ^2CT method, and expressed as fold change in respect to unwounded skin or absolute values for isolated cells.

Whole wounds were collected at 1, 2, and 7 d after wounding and homogenized in 50 mM Tris-HCl, pH 7.5, containing 2 mM EGTA, 1 mM PMSF, 100 KU Aprotinin, 1% Triton X-100 (all from Sigma-Aldrich), and complete protease inhibitor cocktail (Roche). Total proteins were measured by DC Protein Assay, according to manufacturer's instructions (Bio-Rad Laboratories). Mouse PTX3 was measured by ELISA based on the monoclonal antibodies MnmE1 (IgG1) and MnmE2 (IgG1), which were obtained by immunization of $Ptx3^{-/-}$ mice. D-dimer (AMS Biotechnology), PDGF (Bio-Medical Assay Co.), 5-HT (LDN Labor Diagnostika Nord), TGFβ, CD62P, CXCL1, CXCL2, and myeloperoxidase (MPO; R&D Systems) were measured by ELISA in accordance with the manufacturer's instructions. Western blot analysis for Plg/plasmin and Factor II/Thrombin was performed after loading 50 or 20 µg of wound protein extracts on SDS-PAGE (10% acrylamide). The goat polyclonal anti-Plg Kringle 5 (0.5 µg/ml; R&D Systems) and anti-Factor II/thrombin (0.2 µg/ml; R&D Systems) were used. The monoclonal anti-vinculin (0.2 µg/ml; hVIN-1; Sigma-Aldrich) was used as loading control. Plg, plasmin, thrombin, or fibrin bands were quantified by Fiji-ImageJ (ImageJ; NIH) as a ratio of mean gray intensity values of each protein relative to vinculin bands, or as absolute values.

Microtiter binding assay

Binding assays were performed as previously described (Sahni and Francis, 2000; Jeannin et al., 2005). In brief, 96-well plates (Nunc) were coated overnight with 100 ng/50 µl of purified FG, Glu-Plg, Plg fragments, Factor II/Thrombin, Factor III, Factor VII, Factor XIV, αVβ3, Annexin II, PAI-1, or OmpA diluted in PBS^{2+} (containing 130 mg/l $CaCl_2$ and 100 mg/l $MgCl_2$; Lonza). For fibrin-coated wells, 1 U/ml of thrombin (Sigma-Aldrich) was added to 1 mg/ml FG diluted in PBS^{2+}. The solution was mixed, rapidly poured in 96-well plates and, after 45 s, before polymerization, aspirated, leaving a thin film of fibrin coating on the surface. Nonspecific binding to the plates was blocked by incubation for 2 h at 25°C with 0.5% dry milk in PBS^{2+} before incubation (1 h at 25°C) with 100 µl of PTX3, biotin-conjugated C and N domain or biotin-conjugated PTX3 (b-PTX3; 3.5–222 nM) in PBS^{2+} (at indicated pH) containing 0.05% (vol/vol) Tween 20. After washing, PTX3, C and N domain, or bPTX3 were detected by incubation with 100 µl of purified polyclonal rabbit antibody (500 ng/ml) followed by horseradish peroxidase-linked secondary antibody (GE Healthcare) or with 100 µl of horseradish peroxidase-linked avidin (BioSpa). Absorbance values were measured at 450 nm after addition of tetramethylbenzidine substrate (TMB; Sigma-Aldrich). A similar protocol was used for CRP (EMD Millipore) and Plg (EMD Millipore) binding to fibrin. A rabbit polyclonal antibody anti-CRP (EMD Millipore) and a mouse monoclonal anti-Plg (IgG1; AbCam) were used, respectively. In different series of binding experiments, Plg and/or PTX3, CRP, and BSA (Sigma-Aldrich) were, respectively co-incubated with PTX3 or Plg.

Before binding experiments, CRP and the PTX3 C-terminal domain were cross-linked with BS3 (Bis[sulfosuccinimidyl]suberate; Thermo Fisher Scientific) according to the manufacturer's instructions (Bottazzi et al., 1997).

PTX3 binding to conidia of *Aspergillus fumigatus* was performed as previously described (Garlanda et al., 2002) at different pHs.

Surface plasmon resonance

The ProteOn XPR36 Protein Interaction Array system (Bio-Rad Laboratories), based on surface plasmon resonance (SPR) technology, was used for binding studies. Plg was immobilized onto one cell surface of a ProteOn GLC sensor chip (Bio-Rad Laboratories), using amine-coupling chemistry. In brief, the surface was activated for 5 min with a mixture of EDC (0.2 M) and sulfo-NHS (0.05 M), and then Plg was diluted to 30 µg/ml in acetate buffer pH 5.0 and flowed for 5 min at a rate of 30 µl/min. The remaining activated groups were blocked with a 5-min injection of 1 M ethanolamine. The immobilization level was ∼6,500–7,000 resonance units (RU; 1 RU = 1 pg protein/mm^2). Full-length PTX3, its C and N domain were injected over immobilized Plg at a rate of 30 µl/min for 10 min (association phase). To exclude mass transport artifacts, the experiment was also performed changing the flow rate to 100 µl/min. Dissociation phase was measured in the following 15 min. The analyte running buffer was PBS^{2+} at pH 6.0 or pH 7.4, containing 150 mM NaCl and 0.005% (vol/vol) Tween 20. Alternatively, PTX3 and its domains were covalently immobilized as previously described (Deban et al., 2010). In brief, after the activation step, the different ligands were diluted to a final concentration of 30 µg/ml in acetate buffer (pH 2.5–3.0 for PTX3 and N domain PTX3; 4.0 for C domain PTX3). The amounts of PTX3 and C and N domain of PTX3 covalently immobilized onto the surface were ∼3,000, 1,000, and 2,000 RU, respectively. After 90 degree rotation of the fluidic system, Plg was diluted in running buffer (PBS^{2+} pH 6.0) and injected over immobilized ligands at a rate of 30 µl/min, for 5 min (association phase), whereas dissociation was followed for 10 min. The sensorgrams (time course of the SPR signal in RU) were normalized to a baseline value of 0. The resulting sensorgrams were fitted using the simplest 1:1 interaction model (Langmuir model; ProteOn analysis software) to obtain the corresponding association and dissociation rate constants (K_{on} and K_{off}). To determine the affinity of a single molecule of Plg to a single binding site of PTX3, the experiment was also performed flowing Plg (monomeric) onto immobilized PTX3 (octameric) and the N domain (tetramer; Inforzato et al., 2010). Binding constants were calculated considering PTX3 as an octamer, the N domain as a tetramer, and the C domain as a monomer (Inforzato et al., 2010).

Collagen

The collagen content of damaged liver and lung was measured with a conventional OHpro method (Tager et al., 2004). In brief, organs were homogenized in 1 ml of PBS^{2+}, and a 0.5 ml aliquot was hydrolyzed in 6 N HCl at 110°C for 12 h. 25-µl aliquots were added to 0.5 ml of 1.4% chloramine T (Sigma-Aldrich), 10% n-propanol, and 0.5 M sodium acetate. After 20 min of incubation at room temperature, 0.5 ml of Erlich's solution (1 M p-dimethylaminobenzaldehyde [Sigma-Aldrich] in 70% n-propanol, 20% perchloric acid) was added and a 15-min incubation at 65°C was performed. Absorbance was measured at 550 nm and the amount of OH-pro was determined against a standard curve. Sirius red staining is described in the Histology section.

In vitro fibrinolysis models

For cell-free studies, as previously described (Hiraoka et al., 1998), fibrin gels (50 µg each) previously prepared by mixing FG (1 mg/ml) and thrombin (1 U/ml), were incubated in 50 mM Tris, 0.01% (vol/vol) Tween 20, pH 6.0, with the following purified proteins, and combinations thereof: Plg (1 µg/100 µl), uPA (1 ng/100 µl), tPA (1 ng/100 µl), and PTX3 (100 ng/100 µl). After a 16-h incubation at 37°C, fibrin gels were suspended in reducing buffer and proteolysis was assessed in 2 µl of sample by Western blot (see below).

For pericellular fibrinolysis studies, WT and *Ptx3*$^{-/-}$ peritoneal macrophages and mouse embryonic fibroblasts (MEF) were embedded in fibrin gels (3×10^5/ml) as previously described (Carmeliet et al., 1994; Hiraoka et al., 1998). In brief, cells were dissociated with trypsin and centrifuged at 1,000 rpm for 5 min and cell pellet resuspended in a mixture of 2.5 mg/ml of Plg-free FG. Thrombin (1 U/ml) was then added and the suspension was immediately poured into a 24-multiwell plate (300 µl/well) on rounded glasses. The plate was incubated for 30 min at 37°C to allow fibrin polymerization. After washing with PBS^{2+}, fibrin cultures were incubated with 1 ml/well of complete RPMI 1640 in triplicate at 37°C. Cell fibrinolytic activity was evaluated by quantifying fibrinolysis-derived products released in the medium by ELISA, Western blot and by microscopy (see Confocal and two-photon microscopy section). In brief, 96-well plates were coated overnight with the supernatants diluted 1:10^4 in PBS^{2+}. Nonspecific binding was blocked by incubation for 2 h at 25°C with 0.5% dry milk in PBS^{2+} before incubation (1 h at 25°C) with 100 µl of a purified rabbit polyclonal antibody anti-fibrin (ogen) (500 ng/ml; Dako or EMD Millipore) followed by horseradish peroxidase-linked secondary antibody (GE Healthcare) and TMB substrate (Sigma-Aldrich). Values are expressed as mean O.D. ± SD of triplicates. Soluble fibrinolysis products (3 µl of each sample) were also resolved under reducing conditions on 4–12% SDS-PAGE Criterion XT Precast gels (Bio-Rad Laboratories) and detected with polyclonal antibodies anti-fibrin(ogen).

Histology and assessment of tissue sections

For histological analysis, 5-µm-thick paraffin-embedded skin, liver and carotid artery sections were stained with hematoxylin and eosin (H&E) and with Sirius red. Specimens were imaged with an Olympus BX51 microscope equipped with a 2× (N. A. 0.06), 4× (N. A. 0.10), 20× (N. A. 0.4) objectives and with an Olympus XC50 camera. The thickness of wounded skin clot and scab, epithelial gap segment and necroinflammatory area of injured livers were measured in different regions of interest of each single image as segments or free-hand area drawing and quantified using ImageJ (NIH). Count of recruited cells was performed in 3–5 fields (0.05 mm^2) per section. An Olympus dotSlide BX virtual slide scanner equipped with a 10× N.A. 0.25 objective and with a Peltier cooled camera (1376 × 1032 pixels) was used to acquire the entire injured liver specimens. The OlyVIA (version 3.5; Olympus) image software was used to count occluded central veins in the entire section. For quantitative analysis of Sirius red-stained collagen and α-smooth muscle actin; (α-SMA) in skin and liver, 2–10 serial images from 3–10 mice per group were digitally captured at 100× magnification. Collagen staining, α-SMA$^+$ and fibrin in lung and liver immunoreactive areas were measured using the computer-assisted digital image processing software Image-Pro Plus (version 7.0; MediaCybernetics). The total stained area was automatically selected on the basis of RGB color segmentation and results are expressed as mean percentage of the immunoreactive area ± SD.

Flow cytometry

A single-cell suspension of wounded skin was generated by cutting samples into small pieces and digestion in PBS (pH 7.4) supplemented with collagenase type I (1 mg/ml; Sigma-Aldrich) and hyaluronidase (125 U/ml; Sigma-Aldrich) at 37°C for 1 h twice. Finally, a single-cell suspension was obtained by mechanical separation followed by 100 µm filtration and erythrocytes lysis (0.15 M NH_4Cl, 10 nM $KHCO_3$, 1 nM Na_4EDTA, pH 7.2). The following fluorophore-conjugated antibodies were used for immunophenotyping and intracellular staining: anti–mouse CD45 BV605™ (#30-F11; BD) or anti–mouse CD45 BV650 (#A20; BioLegend), anti–mouse CD11b BV421 (#M1/70; BioLegend), anti–mouse Ly6G PE-CF594™ (#1A8; BD), anti–mouse Ly6C FITC™ (#AL-21; BD), anti–mouse F4/80 PE/Cy7™ (#BM8; BioLegend), anti–mouse CD3 PerCP-Cy5.5™ (#BM8; BD), anti–mouse CD140A (PDGFRα) BV421 (#APA5; BD), anti–mouse CD31 PerCP-Cy™5.5 (#MEC 13.3; BD), rabbit anti-FAP Pacific Orange (AbCam), anti–mouse α-SMA FITC (#1A4; Sigma-Aldrich), goat anti–mouse PTX3 Alexa Fluor 647 (R&D Systems), and isotype-matched control antibodies. Cells were fixed with 2% PFA in PBS for 10 min, and when indicated permeabilized with BD Cytofix/Cytoperm kit (BD) according with manufacturer's instructions. Cells viability before the fixation and permeabilization was determined with LIVE/DEAD Fixable Aqua Dead Cell Stain kit (Molecular Probes). Flow cytometry was performed using BD LSRFortessa instrument and BD FACSDiva Version 8.0.1 software (BD). Cell sorting was conducted using BD FACSAria III system. The purity of isolated cells was ≥ 98%.

Confocal and two-photon microscopy

5-µm cryostat sections were incubated in 5% of normal goat (Dako) or donkey (Sigma-Aldrich) serum, 2% BSA, 0.1% Triton X-100 (Sigma-Aldrich) in PBS^{2+}, pH 7.4, (blocking buffer) for 1 h at room temperature. Sections were incubated with the following primary antibodies for 2 h at room temperature: affinity-purified rabbit polyclonal IgG anti-PTX3 (1 µg/ml) or affinity purified goat IgG anti-PTX3/TSG-14 (2 µg/ml; R&D Systems); rat monoclonal (IgG2, 2 µg/ml; Cell Sciences) or rabbit polyclonal (prediluted; AbCam) anti-PDGFRα; rat monoclonal anti–mouse CD68 (IgG2a, 1 µg/ml; Hycult Biotech); goat polyclonal anti-uPAR (5 µg/ml; AbCam); goat polyclonal anti-uPA (2 µg/ml; R&D Systems); rabbit polyclonal anti-fibrin(ogen) (5 µg/ml; Dako); rat monoclonal anti-Plg (IgG1, 5 µg/ml; Cell Sciences); rabbit polyclonal anti-collagen I (4 µg/ml; AbCam); mouse monoclonal anti–α-SMA (2 µg/ml; Sigma-Aldrich); goat anti-proteinase activated receptor-1 (PAR1; 1 µg/ml; R&D Systems); rabbit anti-fibroblast activation protein (FAP; 5 µg/ml; AbCam); rat anti-CD45 allophycocyanin (APC; BD); and rat anti-Ly6C FITC (BD). Sections were then incubated for 1 h with Alexa Fluor (488, 594, 647)–conjugated species-specific cross-adsorbed detection antibodies (Molecular Probes). For DNA detection, DAPI (300 nM; Invitrogen) was used. After each step, sections were washed with PBS^{2+}, pH 7.4, containing 0.01% (vol/vol) Tween 20 (washing buffer). Tissues from *Ptx3*$^{-/-}$ mice were used as negative control for PTX3 immunostaining. Sections were mounted with the antifade medium FluorPreserve Reagent (EMD Millipore) and analyzed with an Olympus Fluoview FV1000 laser scanning confocal microscope with 10× (N.A. 0.4) or oil immersion lens 40× (N.A. 1.3). Immunoreactivity of α-SMA, FAP, PAR1, CD45, Ly6C, collagen I, and fibrin in the wounded skin was evaluated as mean ± SD of the intensity grayscale levels of confocal images (1024 × 1024) obtained with 10×, 20×, or 40× lens, analyzing the whole field of view by FV10-ASW software (version 4.1a; Olympus). For fibrin, 2–5 10× and for Plg, 2–5 40× images/mouse were acquired. Colocalization analysis was performed on confocal images acquired with oil immersion PLAPO 60× lens (N.A. 1.35) at resolution of 1 AU. Overlay RGB images (1024 × 1024; 4–6 images from 5 wounded skins) were imported to Imaris software assembled and colocalization was evaluated by Coloc module by Imaris (Bitplane AG). In all images, the same threshold fluorescence intensity for each channel was fixed, a binary mask of mask colocalization was created and the percentage of colocalization material and the Pearson's index of linear correlation were analyzed. MEF fibrin cultures were fixed in 4% paraformaldehyde, and incubated with polyclonal antibodies anti-fibrin(ogen) and PTX3 and fluorophore-linked secondary antibodies (Invitrogen). Specimens were analyzed with an Olympus Fluoview FV1000 laser scanning confocal microscope in a channel mode with 405, 488, 559, and 635 nm excitations. The resulting fluorescence emissions were collected using a 425–475 nm (for DAPI), 500–545 nm (for Alexa Fluor 488), 595–620nm (for Alexa Fluor 594), and 655–755 nm (for Alexa Fluor 647) band-pass filters. Samples were imaged with oil immersion lens 60× (N. A. 1.35) in *xy* optical sections (800 × 800 pixels) of 0.75 µm. For fibrin cultures, the *z*-stacks were acquired at a resolution of 1 AU to allow three-dimensional reconstruction and presented as three-dimensional projections by Imaris software (X64, version 7.2.1; Bitplane AG).

For ex vivo imaging experiments of pH quantification in the skin, 2-Photon microscopy and the pH-sensitive fluorescent probe 2', 7'-bis-(2-carboxyethyl)-5-(and-6)-carboxyfluorescein (BCECF; Molecular Probes)

were used as described (Hanson et al., 2002). BCECF reports the local pH through a shift in the excitation spectrum and change in the intensity/spectrum of emission as the probe passes from an acid (protonated) to a basic (unprotonated) form. These spectral changes are accompanied by a change in the fluorescence lifetime. 8-wk-old 129/Sv female mice were shaved on the back using a mechanical trimmer and depilatory cream. Two days after wounding with a 6-mm-diam biopsy punch, animals were anesthetized with i.p. injection of 2.5% Avertin and BCECF (acid; 80 µM in ethanol) was applied topically, as previously described (Hanson et al., 2002). After 3 applications within 1 h, whole back skin was removed and stretched on a Petri dish. Images were acquired from the epidermis to the dermis with a LaVision TriM Scope II (LaVision BioTec) two-photon laser-scanning microscope equipped with a 20× (XLUMPFL N.A. 1.0; Olympus) water immersion lens and FLIM X16 TCSPC detector (LaVision BioTec). Excitation was performed using a Chameleon Ultra II (Coherent) laser at 820 nm output. Acquisitions were 400 × 400 µm, 0.78 µm resolution x-y and 5 µm voxel depth, 10 slices. For each mouse, 2–5 acquisitions of both unwounded and wounded areas were performed. Values of pH in dermis were obtained in the depth range of 10–20 µm (Hanson et al., 2002). To exclude possible artifacts due to autofluorescence from hemoglobin present in the clot, acquisitions were performed as indicated in between perilesion area and the ulcer. FLIM z-stacks were imported into Imspector Pro (LaVision BioTec) and fitted to lifetime images. An off-peak time gate was set, to reduce the contribution from SHG. Lifetimes were corrected for instrumentation effects and skin refractive index and calculated as previously described (Hanson et al., 2002). Mean refractive index at all acquisition depths was calculated by measuring the mean lifetime of Coumarin 314 (Sigma-Aldrich). This gave a mean 1.1-fold correction for lifetimes measured in skin, in accordance with the literature (Hanson et al., 2002). The pH at each depth was calculated as a fraction of contributions from lifetime of HBCECF and BCECF.

Specific antibodies and correspondent irrelevant IgGs, were conjugated with Cascade Blue dye and Alexa Fluor fluorophores with Alexa Fluor antibody labeling kits (Invitrogen-Molecular Probes). 8-wk-old 129/Sv female mice were s.c. injected 4 h before acquisition with 200 µl/mouse of Cascade Blue-conjugated rabbit ant-fibrin(ogen; 50 µg/ml), Alexa Fluor 568-conjugated rat anti-Plg (75 µg/ml) and Alexa Fluor 647-conjugated goat anti-Ptx3 (75 µg/ml), or with irrelevant controls. *Ptx3*$^{-/-}$ mice were further used a negative control. BCECF (80 µM in ethanol) was applied topically and skin collected as described before. To avoid the interference of endogenous autofluorescence of the epidermis, the skin sample was then reversed, stretched on a Petri dish and fat and blood were removed with synthetic absorption triangles (Fine Science Tools). Multifluorescent images were acquired on reversed skin samples from the panniculus carnosus to the dermis, excluding the epidermis. Images were acquired using LaVision TriM Scope II microscope with the excitation laser at wavelength 800 nm. Fluorescence emission was collected with the photomultipliers H6780-20, H6780-01, and H7422 (Hamamatsu). Filter configuration was as follows: 420/50, LP493, 525/50, LP593, 609/54, LP625, and 655/40 (Chroma Technologies). Image acquisition, fitting lifetimes, and conversion to pH images were performed using Imspector Pro (LaVision BioTec) and a python algorithm derived from Hanson et al. (2002). Raw image stacks (200 × 200 µm, 0.48 µm pixel resolution in x–y plane and 10 µm voxel depth, 20–50 slices) were imported into Fiji-ImageJ (ImageJ) and 3D mosaics were assembled with Image Stitching plugin. Pearson's r coefficients in the different regions of the reconstructed images were then calculated with Coloc module by Imaris (Bitplane). Statistical analysis was performed with Prism 5 (GraphPad).

Statistical analysis

Results are expressed as mean ± SD or SEM, as specified. Statistical significance between groups was assessed by unpaired two-tailed Mann-Whitney test or Student's *t* test with Prism software (version 4.00 for Windows; GraphPad).

Online supplemental material

Fig. S1 showing the gating strategy used in flow cytometry analysis for immunophenotyping and sorting leukocytes and stromal cells in the course of skin repair, and Fig. S2 showing the method used to measure the pH in wounded skin by two-photon microscopy. Online supplemental material is available at http://www.jem.org/cgi/content/full/jem.20141268/DC1.

We are grateful to the contribution of I. Cuccovillo for the help in animal experiments, and of Achille Anselmo, and Paolo Somma for flow cytometry analysis.

The financial supports of the European Research Council (ERC; to A. Montavoni), the European Commission (FP7-HEALTH-2011-ADITEC-280873), the Italian Association for Cancer Research (AIRC; and AIRC 5x1000), the Italian Ministry of Health and University and Fondazione CARIPLO (Project 2009-2582) are gratefully acknowledged.

A. Montavoni, B. Bottazzi, and C. Garlanda are inventors of patents concerning PTX3 and receive royalties from the sale of PTX3-related reagents. The authors have no additional financial interests.

Author contributions: A. Doni played a key role in designing and conducting most experiments, in particular imaging and animal models, and drafted the manuscript. M. Sironi and S. Valentino prepared reagents and performed biochemical assays. T. Musso, C. Castagnoli, I. Cambieri, and F. Pasqualini performed histological analysis of the skins. D. Morone provided technological support to the two-photon microscopy analyses. V. Zambelli performed the model of acid-induced lung injury. A. Bostone, M. Stravalaci performed the analysis of protein interactions by SPR. S. Tartari, V. Maina, and I. Laface performed histological analysis of liver and lung. A. Ponzetta performed flow cytometry. S.S. Barbieri, E. Tremoli, A.L. Catapano, and G.D. Norata performed the thrombus model. B. Bottazzi and C. Garlanda supervised the project and contributed to drafting the paper. A. Mantovani contributed to the experimental design and supervision of the study, suggested the general link between microbe and matrix recognition and drafted the final version of the paper.

Submitted: 3 July 2014
Accepted: 22 April 2015

REFERENCES

Barbieri, S.S., P. Amadio, S. Gianellini, E. Tarantino, E. Zacchi, F. Veglia, L.R. Howe, B.B. Weksler, L. Mussoni, and E. Tremoli. 2012. Cyclooxygenase-2-derived prostacyclin regulates arterial thrombus formation by suppressing tissue factor in a sirtuin-1-dependent-manner. *Circulation*. 126:1373–1384. http://dx.doi.org/10.1161/CIRCULATIONAHA.112.097295

Bottazzi, B., V. Vouret-Craviari, A. Bastone, L. De Gioia, C. Matteucci, G. Peri, F. Spreafico, M. Pausa, C. D'Ettorre, E. Gianazza, et al. 1997. Multimer formation and ligand recognition by the long pentraxin PTX3. Similarities and differences with the short pentraxins C-reactive protein and serum amyloid P component. *J. Biol. Chem.* 272:32817–32823. http://dx.doi.org/10.1074/jbc.272.52.32817

Bottazzi, B., A. Doni, C. Garlanda, and A. Mantovani. 2010. An integrated view of humoral innate immunity: pentraxins as a paradigm. *Annu. Rev. Immunol.* 28:157–183. http://dx.doi.org/10.1146/annurev-immunol-030409-101305

Bugge, T.H., K.W. Kombrinck, M.J. Flick, C.C. Daugherty, M.J. Danton, and J.L. Degen. 1996. Loss of fibrinogen rescues mice from the pleiotropic effects of plasminogen deficiency. *Cell.* 87:709–719. http://dx.doi.org/10.1016/S0092-8674(00)81390-2

Calvaruso, V., S. Maimone, A. Gatt, E. Tuddenham, M. Thursz, M. Pinzani, and A.K. Burroughs. 2008. Coagulation and fibrosis in chronic liver disease. *Gut*. 57:1722–1727. http://dx.doi.org/10.1136/gut.2008.150748

Camozzi, M., M. Rusnati, A. Bugatti, B. Bottazzi, A. Mantovani, A. Bastone, A. Inforzato, S. Vincenti, L. Bracci, D. Mastroianni, and M. Presta. 2006. Identification of an antiangiogenic FGF2-binding site in the N terminus of the soluble pattern recognition receptor PTX3. *J. Biol. Chem.* 281:22605–22613. http://dx.doi.org/10.1074/jbc.M601023200

Carmeliet, P., L. Schoonjans, L. Kieckens, B. Ream, J. Degen, R. Bronson, R. De Vos, J.J. van den Oord, D. Collen, and R.C. Mulligan. 1994. Physiological consequences of loss of plasminogen activator gene function in mice. *Nature*. 368:419–424. http://dx.doi.org/10.1038/368419a0

Cook, A.D., R. Vlahos, C.M. Massa, E.L. Braine, J.C. Lenzo, A.L. Turner, K.J. Way, and J.A. Hamilton. 2006. The effect of tissue type-plasminogen activator deletion and associated fibrin(ogen) deposition on macrophage localization in peritoneal inflammation. *Thromb. Haemost.* 95:659–667.

Cunha, C., F. Aversa, J.F. Lacerda, A. Busca, O. Kurzai, M. Grube, J. Löffler, J.A. Maertens, A.S. Bell, A. Inforzato, et al. 2014. Genetic PTX3 deficiency and aspergillosis in stem-cell transplantation. *N. Engl. J. Med.* 370:421–432. http://dx.doi.org/10.1056/NEJMoa1211161

de Giorgio-Miller, A., S. Bottoms, G. Laurent, P. Carmeliet, and S. Herrick. 2005. Fibrin-induced skin fibrosis in mice deficient in tissue plasminogen activator. *Am. J. Pathol.* 167:721–732. http://dx.doi.org/10.1016/S0002-9440(10)62046-9

Deban, L., R.C. Russo, M. Sironi, F. Moalli, M. Scanziani, V. Zambelli, I. Cuccovillo, A. Bastone, M. Gobbi, S. Valentino, et al. 2010. Regulation of leukocyte recruitment by the long pentraxin PTX3. *Nat. Immunol.* 11:328–334. http://dx.doi.org/10.1038/ni.1854

Dinarello, C.A. 2009. Immunological and inflammatory functions of the interleukin-1 family. *Annu. Rev. Immunol.* 27:519–550. http://dx.doi.org/10.1146/annurev.immunol.021908.132612

Dyck, R.F., C.M. Lockwood, M. Kershaw, N. McHugh, V.C. Duance, M.L. Baltz, and M.B. Pepys. 1980. Amyloid P-component is a constituent of normal human glomerular basement membrane. *J. Exp. Med.* 152:1162–1174. http://dx.doi.org/10.1084/jem.152.5.1162

Garlanda, C., E. Hirsch, S. Bozza, A. Salustri, M. De Acetis, R. Nota, A. Maccagno, F. Riva, B. Bottazzi, G. Peri, et al. 2002. Non-redundant role of the long pentraxin PTX3 in anti-fungal innate immune response. *Nature.* 420:182–186. http://dx.doi.org/10.1038/nature01195

Gatenby, R.A., and R.J. Gillies. 2004. Why do cancers have high aerobic glycolysis? *Nat. Rev. Cancer.* 4:891–899. http://dx.doi.org/10.1038/nrc1478

Genster, N., M. Takahashi, H. Sekine, Y. Endo, P. Garred, and T. Fujita. 2014. Lessons learned from mice deficient in lectin complement pathway molecules. *Mol. Immunol.* 61:59–68. http://dx.doi.org/10.1016/j.molimm.2014.07.007

Gerold, G., K. Abu Ajaj, M. Bienert, H.J. Laws, A. Zychlinsky, and J.L. de Diego. 2008. A Toll-like receptor 2-integrin beta3 complex senses bacterial lipopeptides via vitronectin. *Nat. Immunol.* 9:761–768. http://dx.doi.org/10.1038/ni.1618

Groeneveld, T.W., M. Oroszlán, R.T. Owens, M.C. Faber-Krol, A.C. Bakker, G.J. Arlaud, D.J. McQuillan, U. Kishore, M.R. Daha, and A. Roos. 2005. Interactions of the extracellular matrix proteoglycans decorin and biglycan with C1q and collectins. *J. Immunol.* 175:4715–4723. http://dx.doi.org/10.4049/jimmunol.175.7.4715

Hamilton, J.A. 1980. Stimulation of macrophage prostaglandin and neutral protease production by phorbol esters as a model for the induction of vascular changes associated with tumor promotion. *Cancer Res.* 40:2273–2280.

Hanington, P.C., and S.M. Zhang. 2011. The primary role of fibrinogen-related proteins in invertebrates is defense, not coagulation. *J. Innate Immun.* 3:17–27. http://dx.doi.org/10.1159/000321882

Hanson, K.M., M.J. Behne, N.P. Barry, T.M. Mauro, E. Gratton, and R.M. Clegg. 2002. Two-photon fluorescence lifetime imaging of the skin stratum corneum pH gradient. *Biophys. J.* 83:1682–1690. http://dx.doi.org/10.1016/S0006-3495(02)73936-2

He, Y.W., H. Li, J. Zhang, C.L. Hsu, E. Lin, N. Zhang, J. Guo, K.A. Forbush, and M.J. Bevan. 2004. The extracellular matrix protein mindin is a pattern-recognition molecule for microbial pathogens. *Nat. Immunol.* 5:88–97. http://dx.doi.org/10.1038/ni1021

Hiraoka, N., E. Allen, I.J. Apel, M.R. Gyetko, and S.J. Weiss. 1998. Matrix metalloproteinases regulate neovascularization by acting as pericellular fibrinolysins. *Cell.* 95:365–377. http://dx.doi.org/10.1016/S0092-8674(00)81768-7

Holmskov, U., S. Thiel, and J.C. Jensenius. 2003. Collections and ficolins: humoral lectins of the innate immune defense. *Annu. Rev. Immunol.* 21:547–578. http://dx.doi.org/10.1146/annurev.immunol.21.120601.140954

Idell, S. 2003. Coagulation, fibrinolysis, and fibrin deposition in acute lung injury. *Crit. Care Med.* **31**(4, Suppl):S213–S220. http://dx.doi.org/10.1097/01.CCM.0000057846.21303.AB

Inforzato, A., C. Baldock, T.A. Jowitt, D.F. Holmes, R. Lindstedt, M. Marcellini, V. Rivieccio, D.C. Briggs, K.E. Kadler, A. Verdoliva, et al. 2010. The angiogenic inhibitor long pentraxin PTX3 forms an asymmetric octamer with two binding sites for FGF2. *J. Biol. Chem.* 285:17681–17692. http://dx.doi.org/10.1074/jbc.M109.085639

Jaillon, S., G. Peri, Y. Delneste, I. Frémaux, A. Doni, F. Moalli, C. Garlanda, L. Romani, H. Gascan, S. Bellocchio, et al. 2007. The humoral pattern recognition receptor PTX3 is stored in neutrophil granules and localizes in extracellular traps. *J. Exp. Med.* 204:793–804. http://dx.doi.org/10.1084/jem.20061301

Jaillon, S., F. Moalli, B. Ragnarsdottir, E. Bonavita, M. Puthia, F. Riva, E. Barbati, M. Nebuloni, L. Cvetko Krajinovic, A. Markotic, et al. 2014. The humoral pattern recognition molecule PTX3 is a key component of innate immunity against urinary tract infection. *Immunity.* 40:621–632. http://dx.doi.org/10.1016/j.immuni.2014.02.015

Jeannin, P., B. Bottazzi, M. Sironi, A. Doni, M. Rusnati, M. Presta, V. Maina, G. Magistrelli, J.F. Haeuw, G. Hoeffel, et al. 2005. Complexity and complementarity of outer membrane protein A recognition by cellular and humoral innate immunity receptors. *Immunity.* 22:551–560. http://dx.doi.org/10.1016/j.immuni.2005.03.008

Koschnick, S., S. Konstantinides, K. Schäfer, K. Crain, and D.J. Loskutoff. 2005. Thrombotic phenotype of mice with a combined deficiency in plasminogen activator inhibitor 1 and vitronectin. *J. Thromb. Haemost.* 3:2290–2295. http://dx.doi.org/10.1111/j.1538-7836.2005.01479.x

Law, R.H., T. Caradoc-Davies, N. Cowieson, A.J. Horvath, A.J. Quek, J.A. Encarnacao, D. Steer, A. Cowan, Q. Zhang, B.G. Lu, et al. 2012. The X-ray crystal structure of full-length human plasminogen. *Cell Reports.* 1:185–190. http://dx.doi.org/10.1016/j.celrep.2012.02.012

Lech, M., C. Römmele, R. Gröbmayr, H. Eka Susanti, O.P. Kulkarni, S. Wang, H.J. Gröne, B. Uhl, C. Reichel, F. Krombach, et al. 2013. Endogenous and exogenous pentraxin-3 limits postischemic acute and chronic kidney injury. *Kidney Int.* 83:647–661. http://dx.doi.org/10.1038/ki.2012.463

Lin, Q., D. Fang, J. Fang, X. Ren, X. Yang, F. Wen, and S.B. Su. 2011. Impaired wound healing with defective expression of chemokines and recruitment of myeloid cells in TLR3-deficient mice. *J. Immunol.* 186:3710–3717. http://dx.doi.org/10.4049/jimmunol.1003007

Lu, J., L.L. Marnell, K.D. Marjon, C. Mold, T.W. Du Clos, and P.D. Sun. 2008. Structural recognition and functional activation of FcgammaR by innate pentraxins. *Nature.* 456:989–992. http://dx.doi.org/10.1038/nature07468

Lund, L.R., K.A. Green, A.A. Stoop, M. Ploug, K. Almholt, J. Lilla, B.S. Nielsen, I.J. Christensen, C.S. Craik, Z. Werb, et al. 2006. Plasminogen activation independent of uPA and tPA maintains wound healing in gene-deficient mice. *EMBO J.* 25:2686–2697. http://dx.doi.org/10.1038/sj.emboj.7601173

Ma, Y.J., A. Doni, L. Romani, H.J. Jürgensen, N. Behrendt, A. Mantovani, and P. Garred. 2013. Ficolin-1-PTX3 complex formation promotes clearance of altered self-cells and modulates IL-8 production. *J. Immunol.* 191:1324–1333. http://dx.doi.org/10.4049/jimmunol.1300382

Martinez, F.O., L. Helming, and S. Gordon. 2009. Alternative activation of macrophages: an immunologic functional perspective. *Annu. Rev. Immunol.* 27:451–483. http://dx.doi.org/10.1146/annurev.immunol.021908.132532

Maugeri, N., P. Rovere-Querini, M. Slavich, G. Coppi, A. Doni, B. Bottazzi, C. Garlanda, D. Cianflone, A. Maseri, A. Mantovani, and A.A. Manfredi. 2011. Early and transient release of leukocyte pentraxin 3 during acute myocardial infarction. *J. Immunol.* 187:970–979. http://dx.doi.org/10.4049/jimmunol.1100261

Medzhitov, R. 2008. Origin and physiological roles of inflammation. *Nature.* 454:428–435. http://dx.doi.org/10.1038/nature07201

Mitchell, C., D. Couton, J.P. Couty, M. Anson, A.M. Crain, V. Bizet, L. Rénia, S. Pol, V. Mallet, and H. Gilgenkrantz. 2009. Dual role of CCR2 in the constitution and the resolution of liver fibrosis in mice. *Am. J. Pathol.* 174:1766–1775. http://dx.doi.org/10.2353/ajpath.2009.080632

Nakayama, Y., S. Kon, D. Kurotaki, J. Morimoto, Y. Matsui, and T. Uede. 2010. Blockade of interaction of alpha9 integrin with its ligands hinders the formation of granulation in cutaneous wound healing. *Lab. Invest.* 90:881–894. http://dx.doi.org/10.1038/labinvest.2010.69

Napoleone, E., A. Di Santo, A. Bastone, G. Peri, A. Mantovani, G. de Gaetano, M.B. Donati, and R. Lorenzet. 2002. Long pentraxin PTX3 upregulates tissue factor expression in human endothelial cells: a novel link between vascular inflammation and clotting activation. *Arterioscler. Thromb. Vasc. Biol.* 22:782–787. http://dx.doi.org/10.1161/01.ATV.0000012282.39306.64

Norata, G.D., P. Marchesi, V.K. Pulakazhi Venu, F. Pasqualini, A. Anselmo, F. Moalli, I. Pizzitola, C. Garlanda, A. Mantovani, and A.L. Catapano. 2009. Deficiency of the long pentraxin PTX3 promotes vascular

inflammation and atherosclerosis. *Circulation*. 120:699–708. http://dx.doi.org/10.1161/CIRCULATIONAHA.108.806547

Nurden, A.T. 2011. Platelets, inflammation and tissue regeneration. *Thromb. Haemost.* 105):S13–S33. http://dx.doi.org/10.1160/THS10-11-0720

Pepys, M.B., and G.M. Hirschfield. 2003. C-reactive protein: a critical update. *J. Clin. Invest.* 111:1805–1812. http://dx.doi.org/10.1172/JCI200318921

Pohl, J.F., H. Melin-Aldana, G. Sabla, J.L. Degen, and J.A. Bezerra. 2001. Plasminogen deficiency leads to impaired lobular reorganization and matrix accumulation after chronic liver injury. *Am. J. Pathol.* 159:2179–2186. http://dx.doi.org/10.1016/S0002-9440(10)63069-6

Proctor, R.A. 1987. Fibronectin: an enhancer of phagocyte function. *Rev. Infect. Dis.* 9(Suppl 4):S412–S419. http://dx.doi.org/10.1093/clinids/9.Supplement_4.S412

Ricklin, D., and J.D. Lambris. 2013. Complement in immune and inflammatory disorders: pathophysiological mechanisms. *J. Immunol.* 190:3831–3838. http://dx.doi.org/10.4049/jimmunol.1203487

Rodriguez-Grande, B., M. Swana, L. Nguyen, P. Englezou, S. Maysami, S.M. Allan, N.J. Rothwell, C. Garlanda, A. Denes, and E. Pinteaux. 2014. The acute-phase protein PTX3 is an essential mediator of glial scar formation and resolution of brain edema after ischemic injury. *J. Cereb. Blood Flow Metab.* 34:480–488. http://dx.doi.org/10.1038/jcbfm.2013.224

Romer, J., T.H. Bugge, C. Pyke, L.R. Lund, M.J. Flick, J.L. Degen, and K. Dano. 1996. Impaired wound healing in mice with a disrupted plasminogen gene. *Nat. Med.* 2:287–292. http://dx.doi.org/10.1038/nm0396-287

Sahni, A., and C.W. Francis. 2000. Vascular endothelial growth factor binds to fibrinogen and fibrin and stimulates endothelial cell proliferation. *Blood.* 96:3772–3778.

Salio, M., S. Chimenti, N. De Angelis, F. Molla, V. Maina, M. Nebuloni, F. Pasqualini, R. Latini, C. Garlanda, and A. Mantovani. 2008. Cardioprotective function of the long pentraxin PTX3 in acute myocardial infarction. *Circulation.* 117:1055–1064. http://dx.doi.org/10.1161/CIRCULATIONAHA.107.749234

Schack, L., R. Stapulionis, B. Christensen, E. Kofod-Olsen, U.B. Skov Sørensen, T. Vorup-Jensen, E.S. Sørensen, and P. Höllsberg. 2009. Osteopontin enhances phagocytosis through a novel osteopontin receptor, the alphaXbeta2 integrin. *J. Immunol.* 182:6943–6950. http://dx.doi.org/10.4049/jimmunol.0900065

Schäfer, M., and S. Werner. 2008. Cancer as an overhealing wound: an old hypothesis revisited. *Nat. Rev. Mol. Cell Biol.* 9:628–638. http://dx.doi.org/10.1038/nrm2455

Schneider, L.A., A. Korber, S. Grabbe, and J. Dissemond. 2007. Influence of pH on wound-healing: a new perspective for wound-therapy? *Arch. Dermatol. Res.* 298:413–420. http://dx.doi.org/10.1007/s00403-006-0713-x

Semple, J.W., J.E. Italiano Jr., and J. Freedman. 2011. Platelets and the immune continuum. *Nat. Rev. Immunol.* 11:264–274. http://dx.doi.org/10.1038/nri2956

Singer, A.J., and R.A. Clark. 1999. Cutaneous wound healing. *N. Engl. J. Med.* 341:738–746. http://dx.doi.org/10.1056/NEJM199909023411006

Subramaniam, M., S. Saffaripour, L. Van De Water, P.S. Frenette, T.N. Mayadas, R.O. Hynes, and D.D. Wagner. 1997. Role of endothelial selectins in wound repair. *Am. J. Pathol.* 150:1701–1709.

Suresh, M.V., S.K. Singh, and A. Agrawal. 2004. Interaction of calcium-bound C-reactive protein with fibronectin is controlled by pH: in vivo implications. *J. Biol. Chem.* 279:52552–52557. http://dx.doi.org/10.1074/jbc.M409054200

Tager, A.M., R.L. Kradin, P. LaCamera, S.D. Bercury, G.S. Campanella, C.P. Leary, V. Polosukhin, L.H. Zhao, H. Sakamoto, T.S. Blackwell, and A.D. Luster. 2004. Inhibition of pulmonary fibrosis by the chemokine IP-10/CXCL10. *Am. J. Respir. Cell Mol. Biol.* 31:395–404. http://dx.doi.org/10.1165/rcmb.2004-0175OC

Tomita, H., Y. Iwata, F. Ogawa, K. Komura, K. Shimizu, A. Yoshizaki, T. Hara, E. Muroi, K. Yanaba, S. Bae, et al. 2009. P-selectin glycoprotein ligand-1 contributes to wound healing predominantly as a p-selectin ligand and partly as an e-selectin ligand. *J. Invest. Dermatol.* 129:2059–2067. http://dx.doi.org/10.1038/jid.2008.446

Wong, C.H., C.N. Jenne, B. Petri, N.L. Chrobok, and P. Kubes. 2013. Nucleation of platelets with blood-borne pathogens on Kupffer cells precedes other innate immunity and contributes to bacterial clearance. *Nat. Immunol.* 14:785–792. http://dx.doi.org/10.1038/ni.2631

Yukami, T., M. Hasegawa, Y. Matsushita, T. Fujita, T. Matsushita, M. Horikawa, K. Komura, K. Yanaba, Y. Hamaguchi, T. Nagaoka, et al. 2007. Endothelial selectins regulate skin wound healing in cooperation with L-selectin and ICAM-1. *J. Leukoc. Biol.* 82:519–531. http://dx.doi.org/10.1189/jlb.0307152